

TEL AVIV אוניברסיטת
UNIVERSITY תל אביב

הפקולטה למדעים מדויקים ע"ש ריימונד ובברלי סאקלר

בית הספר לפיסיקה ואסטרונומיה

המחלקה לחומר מעובה

Tunable All-Dielectric Metasurfaces in the Mid-Infrared

In partial fulfillment to the requirements for the degree of

Master of Science at Tel Aviv University

School of Physics & Astronomy,

Department of Condensed Matter Physics

By

Omri Meron

March 2020

Under the supervision of Prof. Haim Suchowski

Acknowledgments

I wish to express my gratitude to my supervisor, Prof. Haim Suchowski, for his guidance and support during this project. I would like to thank the femto-nano group, for their friendship and support. Special appreciation to M.Sc Uri Arieli for taking me under his professional care during the early stages of my Master.

Advanced technological capabilities to fabricate materials in subwavelength scales gave rise to the field of metamaterials which revolutionized light matter interaction studies in the past few decades. Many diverse research questions have been studied through these metamaterials, but these questions have mostly been restricted to the visible and near infrared spectral regions. The mid infrared region, which encompasses exclusive detection capabilities, from the biochemical fingerprint through blackbody radiation detection and more, has received little attention. This thesis studies the ability to shift metamaterials into the mid infrared spectral region through a relatively new approach referred to as dielectric metamaterials. Compared to previous attempts, dielectric metamaterials undergo very low loss through the use of transparent scatterers as their building blocks. Based on Silicon photonics and through the coupling of electric and magnetic collective dipole resonances, we study a metasurface based analogue of the electromagnetically induced transparency (EIT) phenomenon in the mid infrared. The study involves extensive numerical simulations including near and far field analysis of the system. In addition, we present up to date resonance measurements, centered at $\lambda_r = 2431nm$, with Q-factors exceeding 344, as well as a series of Fano-resonances constructed of various electric and magnetic multipoles varying from the near to mid infrared spectral region. The measurements manifest high resolution resonant wavelength tuning capabilities of up to several nanometers, as well as large shifts, on the scale of hundreds of nanometers, due to fabrication mastery. Finally, the challenges in fabrication and measurement processes are discussed, as well as possible routes chosen to overcome them.

Table of Contents

Nomenclature	v
List of Figures	vii
List of Tables	xv
1: Introduction	1
2: Background	3
2.1 Electromagnetic behavior of ordinary materials	3
2.2 Mie theory	4
2.2.1 Localized surface plasmon resonance	7
2.2.2 Whispering gallery modes	8
2.3 Characterizing a metasurface	10
2.4 Interference between Mie resonances and directional scattering	11
2.4.1 Fano resonance	11
2.5 Electromagnetically induced transparency	12
3: Motivation - Dielectric metasurfaces in the mid IR	17
3.1 Why Dielectric meta surfaces	17
4: Experimental realization	19
4.1 Choosing the constituent materials	19

4.2	FDTD Simulations	20
4.2.1	Bar and disc arrays	20
4.2.2	Electromagnetic induced transparency analogue	22
4.3	Fabrication process	27
4.3.1	E-beam lithography challenges	30
4.3.2	RIE process challenges	31
4.4	Measurement apparatus	32
4.4.1	The MIRcroscope	33
4.5	Measurement results	34
5:	Conclusions	39
	References	41
	Appendix A: Raman scattering from Silicon and Graphene	44
	Appendix B: Methods	46
B.1	Fabrication recipe	46
B.2	FDTD simulations	46
	Appendix C: Designed geometries	48

Nomenclature

CMOS complementary metal-oxide-semiconductor

E-beam electron beam

EIT electromagnetically induced transparency

FDTD finite difference time domain

FS forward scattering

LSPR localized surface plasmon resonance

MDR morphological dependent resonances

MIR mid infrared

NIR near infrared

NSOM near-field scanning optical microscopy

OPO optical parametric oscillator

RBS radar back scattering

RIE reactive ion etching

SC super continuum

SEIRA surface enhanced infrared absorption

SEM scanning electron microscope

SERS surface enhanced Raman spectroscopy

WGM whispering gallery modes

List of Figures

2.1	Lines of force of the first four electric and magnetic partial waves [1]. . .	6
2.2	Plasmonic response of metallic nano-bars. (a)-(c), SEM images of gold nano-bars of different lengths, 115nm, 155nm and 215nm ,respectively. (d) Transmission spectrum of the LSPR absorption lines for varying lengths of gold nano-bars. Figures (a)-(d) where borrowed with consent from the work of a colleague from my lab.	7
2.3	The coupling between two perpendicular nano-bars. (a) View of the spatial arrangement of two gold nano-bars and the polarization of the incident light wave. (b) Transmission spectrum that exhibits the splitting of the single LSPR electric dipole resonance into two shifted resonant lines. (c) SEM image of a fabricated array of the pair coupled particles. (d) Simulation snapshots presenting the spatial distribution of the localized electric field intensity in different time constants. (e) Electric field intensity plots as a function of time for monitors placed in points A (blue) and B (red), see points in (a). (f) A schematic energy level diagram describing the splitting process due to the emergence of a symmetric and anti-symmetric state. Figures (a)-(e) where borrowed with consent from the work of a colleague from my lab.	9
2.4	(a) Representing a metafilm as an effective medium of thickness d. (b) The effective permittivity of a metasurface modeled as an effective medium for different layer thicknesses d (spherical particles with radius of 10 nm , spacing of 25.59 nm , $\epsilon = 2$, and $\mu = 900$ - modeled for radio frequency) [2].	11

2.5	RBS (red) and FS (blue) cross-sections versus normalized frequency ω/ω_p . The dielectric permittivity ϵ is described by the Drude formula for a plasmonic sphere. The calculations follow equations 2.10, 2.11 for a_1 and a_2 only. Inset shows polar scattering diagrams in the $x - z$ plane near the quadrupole resonance of a plasmonic particle. Red lines represent linearly polarized light; blue lines represent non-polarized light [3].	13
2.6	Schematic illustration of a three-level system. $ 1\rangle$ signifies the ground state, $ 3\rangle$ the "bright" state and $ 2\rangle$ the "dark" state. Ω_p donates the Rabi frequency used to probe the "bright" state from the ground state, and Ω_c the coupling Rabi frequency between the "bright" state and the "dark" state. $\Delta = \Delta_p = \Delta_c$ signify the equal detuning in the EIT case.	14
2.7	(a) A typical absorption (α) spectrum ,and (b) an EIT absorption spectrum. In both cases, Δ is the detuning from resonance. The subscript p in (b) signifies that the probe frequency is being scanned [4].	14
2.8	Plasmonic induced transparency (EIT analogue). (a) Top view of the plasmonic system consisting of a radiative element and a dark element with a separation distance d , with light incident at the normal direction. (b) The real and imaginary parts of a \vec{E} probe placed $10nm$ from the end facet of the radiative antenna (red arrow in (a)) for separations ranging from $d = 40$ to $100nm$ between the radiative and dark elements. (c) The 2D field intensity plot of an uncoupled radiative atom (left) and a radiative atom coupled with a dark atom with a separation of $40nm$ (right) at a frequency of $428.4THz$, as indicated by the red triangle in (b) [5].	16
3.1	Two routes for MIR plasmonics: (a) Drude model of real (solid) and imaginary (dashed) permittivity for the three noble metals: Gold (Au), Copper (Cu) and Silver (Ag) [6]. (b) Absorption cross-section simulation of a Boron-type Heavily doped Si particle, with carrier concentrations (N) of over $10^{20}[cm^{-3}]$, geometrical aspect ratio of $1/2$	18

4.1	Left: Silicon (red) on Sapphire EIT analogue metasurface design. $a = 1280nm$, $h = 230nm$, $l = 1022nm$, $w = 347nm$, $R = 369nm$, $g_1 = 85.5nm$, $g_2 = 109.5nm$. The detuning $\Delta = g_2 - g_1$ is the parameter that links the geometry with the coupling strength between the "bright mode" and the "dark mode". Right: Simulation of the resulting EIT transmission, reflection and absorption spectrums. You can clearly see the negligible absorption of this process.	21
4.2	Reflection spectrum (normalized units) of separated bar (orange) and Disc (blue) square lattices with a lattice constant of $1280nm$	21
4.3	Simulated transmission spectrum for varying lattice constants. (a) Bar lattice with a varying horizontal lattice constant. Bar length $1022nm$, width $347nm$ and height $230nm$. The vertical lattice constant for all simulations is $1280nm$. The dipole moment centered at $2250nm$ (for lattice constant $1280nm$) is blue shifted with varying amplitude as the lattice constant shortens. In addition as the lattice constant shortens other high order resonances appear. (b) Disc lattice with a varying lattice constant (vertical and horizontal). Disc radius $400nm$ and height $230nm$. The dipole moment centered at $2250nm$ (for lattice constant $1280nm$) is blue shifted and enhanced as the lattice constant shortens. In addition a magnetic dipole resonance appears.	22
4.4	Near field profile analysis of the symmetric geometry arrangement ($\Delta = 0nm$). (a) Transmission line (blue), and brown marks that specify the 4 wavelength chosen for field profile display. (b-e) Left: Electric field x-y profile positioned in $z = 50nm$. The colorbar indicates $\Re(E_z)$ and red arrows $\Re(E_x, E_y)$. Right: Magnetic field x-y profile positioned in $z = 125nm$. The colorbar indicates $\Re(H_z)$ and red arrows $\Re(H_x, H_y)$. Middle: In every row the upper display is the electric field x-z profile, and lower display the magnetic field x-z profile, both positioned in $y = 0$. The profiles include a caption specifying their excitation wavelength.	23

- 4.5 Near field profile analysis of the EIT analogue, asymmetric geometry arrangement ($\Delta = 24nm$). (a) Transmission line (blue), and brown marks that specify the 6 wavelength chosen for field profile display. (b-e) Left: Electric field profile in $z = 218nm$, colormap indicates $\Re(E_z)$ and red arrows $\Re(E_x, E_y)$. Right: Magnetic field profile in $z = 218nm$, colormap indicates $\Re(H_z)$ and blue arrows $\Re(H_x, H_y)$. Middle: Upper display is the electric field profile, and lower display the magnetic field profile in $y = 0$. The profiles include a caption specifying their excitation wavelength. Points (f)-(g) display profiles similar to the same wavelengths in figure (4.4.b,e). 24
- 4.6 EIT analogue metasurface: (Left) Illustration of the spacial arrangement of discs and bars, electric (red to blue gradient) and magnetic (yellow to green gradient) fields, the color gradient illustrates the phase variance. (Right) Energy diagram consisting of a ground non excited state $|1\rangle$, "bright mode" electric dipole excitation $|3\rangle$, and "dark mode" magnetic dipole excitation $|2\rangle$ due to an asymmetric displacement of the disc between two bars. . . . 25
- 4.7 Simulation of the EIT analogue design from figure (4.1) of four different detuning levels (Δ). Transmission line (blue) and phase (dashed brown). These plots highlight the importance of a coherent structure, where deviations of 10nm in disc position vary the measured spectrum dramatically. . 26
- 4.8 Near field profile analysis of the EIT analogue sample centered at 2960nm, asymmetric geometry arrangement ($\Delta = 24nm$). Simulation for a shorter wavelength excitation centered at $\lambda_r = 2058nm$. Incident polarization aligned with the bar's long axis. (a) Transmission line (blue), and brown marks that specify the 3 wavelength chosen for field profile display. (b-d) Left: Electric field profile in $z = 46nm$, colormap indicates $\Re(E_z)$ and red arrows $\Re(E_x, E_y)$. Right: Magnetic field profile in $z = 103nm$, colormap indicates $\Re(H_z)$ and blue arrows $\Re(H_x, H_y)$. Middle: The magnetic field profile in $x = -436nm$ (aligned with the center of the disc). The profiles include a caption specifying their excitation wavelength. 28

4.9	Near field profile analysis of the EIT analogue sample centered at 3150nm, asymmetric geometry arrangement ($\Delta = 41.5nm$). Simulation for a shorter wavelength excitation centered at $\lambda_r = 1640nm$. Incident polarization perpendicular to the bar's long axis. (a) Transmission line (blue), and brown marks that specify the 3 wavelength chosen for field profile display. (b-d) Left: Electric field profile in $z = 46nm$, colormap indicates $\Re(E_z)$ and red arrows $\Re(E_x, E_y)$. Right: Magnetic field profile in $z = 103nm$, colormap indicates $\Re(H_z)$ and blue arrows $\Re(H_x, H_y)$. Middle: Upper display is the electric field profile, and lower display the magnetic field profile in $y = 0$ plane. The profiles include a caption specifying their excitation wavelength.	29
4.10	Fabrication process illustration - (a) A 230nm Si layer on a Sapphire substrate, spin coated with 340nm ZEP positive resist and 60nm PMMA <i>Electra 92</i> conductive layer. (b) E-beam lithography exposes the area between the designated particles. (c) A reactive ion etching process is used to etch the exposed Silicon layer until the Sapphire layer is reached. (d) After removing the remaining resist we are left with our metasurface design.	30
4.11	SEM images of different fabricated samples: (a) A lattice close up, Dozens of unit cells containing a disk and bar placed alternately in a square lattice. (b) An example of inaccurate fabrication parameters. (c)-(d) Unsuccessfully etched examples from calibration attempts of an isotropic RIE process (while in (h) the <i>SLR770</i> Bosch process was used for the same E-beam lithography parameters). (e)-(f) Example of the first successful fabrication processes. (g)-(h) Example of more precise fabrication processes done lately (i) Higher resonance with a larger geometry are easier to fabricate.	32
4.12	The MIRcroscope: a MIR compatible imaging microscope, consists of two light sources, One self generated coherent tunable mid IR collimated plain wave source for measurements, and a second incoherent visible light source for imaging. After propagating through the sample holder the beam is expanded using a telescope, then passed through an Iris to collect light from a certain sample area. The beam is then split using a pellicle beam splitter to an optical fiber and an imaging system.	33

4.13	A cluster of spectrum measurement plots (a)-(b) Transmission spectrum of a Fano-shaped resonance measured using <i>ORIA IR Femto-second OPO</i> with incident beams centred at $2250nm$ and $2400nm$ respectively. (c) A Fano-Lorentzian fit for the spectrum measured in figure (b). The extracted Q-factor is 344. Notice the wavelength axis was converted to wavenumber. (d) Geometry comparison with similar designs, but minor geometrical changes. (e) Measurement using the SC laser comparing the original EIT geometry from figure 4.1 to separate disc and bar lattices with same unit cell.	35
4.14	Transmission spectrum of measured (orange) and simulated (blue dashed) not fully etched lattices. In addition, an illustration presents the unetched Silicon thin layer on top of the Sapphire substrate.	36
4.15	Transmission spectrum plots of higher EIT analogue designed samples, using the <i>HORIBA</i> spectrometer and the self built tunable MIR source utilizing the <i>MOPO3</i> crystal. All three samples display a small Fano-shaped resonance, shifted by $\sim 400nm$ from its simulated center resonance. (a) Sample designed to resonate in $2960nm$ but is centered instead in $3290nm$. (b) Sample designed to resonate in $3150nm$ but is centered instead in $3480nm$. (c) Sample designed to resonate in $3350nm$ but is centered instead in $3695nm$	37
4.16	Transmission comparison for three different samples (EIT $2960nm$, EIT $3150nm$ and EIT $3350nm$ from figure (4.15)), between simulations and measurements of high multimode Fano-resonant mechanism. (a) and (b) present simulation and measurements, respectively, for resonant mechanism presented in figure (4.8). Incident beam polarized parallel to the bar's long axis. (c) and (d) present simulation and measurements, respectively, for resonant mechanism presented in figure (4.9). Incident beam polarized perpendicular to the bar's long axis. All measurements were conducted using the <i>NIRquest</i> spectrometer and the <i>SC</i> source.	38

A.1	Raman measurements comparison of Si nanostructures and bulk. A colored circle links between design to spectrum line. Excitation energy 2.33eV. An enhancement factor of $\times 20$ is observed using the metasurface design (purple line) referred to bulk measurements (dashed line). We assume the incident light signal undergoes Near field enhancement due to Mie scattering effects in the nanoparticles.	44
A.2	Raman measurements of single and multi-layered Graphene. (a) Measurements of G-band, no sign for D-band what means the Graphene lattice is free of defects. (b) G'-band measurements, the number of Graphene layers is guessed through comparison to publications. (c) Picture of the Graphene sample with marked areas for measurements with matching color to part b. (d) Gaussian fit for single layer Graphene.	45

List of Tables

C.1	EIT analogue unit cell geometrical designs according to figure (4.1). All lengths specified in nanometers.	48
-----	--	----

1 Introduction

The study of light matter interaction has a long and rich history of over 200 years in which electromagnetic material development and applications have blossomed, culminating with the advent of metamaterials. The prefix "meta" is a Greek preposition meaning (among other things) "beyond", which suggests metamaterials are novel, synthetic materials in which light matter interaction can be tailored for a unique desired purpose, "beyond" what exists in natural bulk materials. Realization of metamaterials is usually done by arranging a set of small scatterers in a regular array throughout a region in space, thus obtaining some desirable bulk behaviour.

A simple version of a metamaterial, especially in terms of fabrication, can be arranged in two dimensional space and achieve a satisfying amount of unique properties. Such a version of a metamaterial has been given the name "metasurface". The main advantages metasurfaces have over metamaterials are low loss and compactness, which means they are great candidates for manipulating propagating electromagnetic waves, either by a phase shift or change in amplitude.

Like a metamaterial, the behavior of a metasurface is determined by the electric and magnetic polarizabilities (α) of its constituent scatterers. accordingly, numerous linear potential applications, such as frequency selective surfaces, beam shaping, including focusing, defocusing, reflection, and refraction, polarizing, cloaking devices, optical switches, light harvesting, biomedical sensors and many more [7]. Metasurfaces also have strong nonlinear properties due to the ability to create highly localized electromagnetic fields with desired symmetry properties [8].

Metasurfaces have been mainly investigated in the visible and near infrared (NIR) spectral ranges. A less investigated spectral range of metasurfaces, which comprises tremendous potential is the mid infra red (MIR) range. The MIR which generally varies from $2 - 20\mu m$ encompasses the primary vibrational absorption bands of most bio-chemical molecules and in particular the fingerprint region. The MIR is also where the peak black-

body emission for most biological and mechanical objects can be found (300-1500K) and therefore, essential for thermal imaging. In the field of condensed matter physics the MIR meets the energy levels of some interesting semiconductor bandgaps such as black phosphorous (2D) and InAs, as well as phonon absorption bands.

Most attempts to create MIR metasurfaces in the past two decades have been based on localized surface plasmons as their Resonance mechanism (see section 2.2.1). These metasurfaces will be referred to as plasmonic metasurfaces. There are basically two routes to excite localized surface plasmon resonances (LSPRs) in the MIR: The first is by simply red-shifting the resonant frequency of the widely used noble metal nano-particles by adjusting their morphology, and the second route is by using heavily doped semiconductors as building blocks [9, 6]. Yet, both options suffer from inherent losses due to low carrier mobility in this spectral range.

In recent years there has been a growing interest in the field of dielectric metasurfaces, which are transparent in the MIR and inherently have low loss. Composed of high refractive index materials (such as semi-conductors or ceramics), in transparent regions of the constituent building blocks, these metasurfaces experience Mie resonances with high controlability over phase and amplitude (see section 2.2). The main advantage of dielectric metasurfaces is that they undergo negligible absorption loss with respect to plasmonic metasurfaces. High scattering losses at resonant frequencies that characterize these particles can be circumvented using effects of interference between Mie resonances, which enable the tailoring of directional scattering [10].

The field of dielectric metasurfaces has barely been developed in the MIR region. In this thesis, we have brought the knowledge of MIR based metasurfaces to our laboratory - from numerical simulation, fabrication to experimental measurements. I have focused, as a test case, on a spectrum analogue for the electromagnetically induced transparency (EIT) phenomenon (see section 2.5) in the MIR spectral range. The uniqueness and application of an EIT spectrum is expressed in a large phase delay accumulated by the transmission band, while propagating through the metasurface, in other words creating "slow light". My work will serve as a basis for more extensive future research work in the ultrafast and nonlinear optics domain.

2 Background

Optical metasurfaces are designed to meet specific electromagnetic properties when interacting with light. Although most metasurfaces these days are designed and studied using numerical simulation, one should understand the underlying mechanisms that allow such a great diversity of applications. In this chapter, I will give a short review of Mie scattering theory, the resonant mechanism of subwavelength scattering particles. I will then elaborate on the difficulty to model a metasurface by bulk electromagnetic parameters (using effective medium theory) and offer a plausible solution. Furthermore, I will discuss effects of interference between Mie resonances and under what conditions does this cause directional scattering. Finally I will give an introduction to electromagnetically induced transparency phenomenon. Prior to a discussion on the behavior of engineered materials, let us revisit the fundamental definition for the permittivity (ϵ) and permeability (μ) of a medium.

2.1 *Electromagnetic behavior of ordinary materials*

Permittivity describes the response of the medium to an external electric field due to the induced electric dipole of an ensemble of small scattering particles. Traditionally, these particles have been regarded as atoms or molecules, but in the past two decades, since the development of artificial dielectric materials these scatterers can be considered as meta-atoms – metal or dielectric particles. These man-made structures are much larger than atoms but still smaller than the wavelength of the electromagnetic field in the "host" medium in which these meta-atoms are embedded. In either case, the induced dipole \mathbf{p} is related to the local incident electric field \mathcal{E} acting on a particle by the electric polarizability α :

$$\mathbf{p} = \alpha \mathcal{E}, \quad (2.1)$$

assuming isotropic medium. In order to define the collective polarization density \mathbf{P} and the macroscopic effective electric field \mathbf{E} , the dipole moments as well as the local incident

electric field are volume averaged. From these, the electric displacement vector \mathbf{D} and permittivity (ϵ) are defined by:

$$\mathbf{D} = \epsilon_0 \mathbf{E} + \mathbf{P} = \epsilon \mathbf{E}, \quad (2.2)$$

where ϵ_0 is the vacuum permittivity, and the permittivity ϵ is related to the electric polarizability densities of the scatterers in space.

Permeability can be defined in analogy to the electric case by the volume averaged and auxiliary magnetic fields \mathbf{B} and \mathbf{H} , and by the polarization \mathbf{M} :

$$\mathbf{B} = \mu_0 (\mathbf{H} + \mathbf{M}) = \mu \mathbf{H}, \quad (2.3)$$

where, as before, μ_0 is the vacuum permeability, and the permeability μ is related to the magnetic polarizability density of the scatterers in space. With these macroscopic descriptions, details of the field behavior on the scale of scatterer size and separation are lost. Naturally $\epsilon = \epsilon' + i\epsilon''$ and $\mu = \mu' + i\mu''$ are complex variables. The imaginary contribution ϵ'' and μ'' should have positive values except for active materials [10]. The product of the complex permittivity and permeability defines the squared refractive index $n^2 = \epsilon\mu$. The challenge of defining microscopic parameters for metasurfaces begins by describing the interaction between light and the individual meta-atom. Due to their size, which is not as small as atoms but still subwavelength, Mie-scattering theory is commonly being used.

2.2 Mie theory

In 1908, Gustav Mie, developed his theory in an effort to understand the varied colors in the absorption and scattering exhibited by small colloidal gold particles suspended in water. Mie theory, which describes the scattering of a plane wave by an arbitrary sized homogeneous sphere, has acquired great relevance in the past few years in the emergent branch of nano-optics, which describes the effects of morphological resonances in plasmonics and dielectric nano-structures based on the optics of high refractive index nanoparticles. The term "Mie scattering" refers usually to scattering from a particle which size d is comparable or smaller than the wavelength of light in the surrounding medium ($\lambda \geq d$).

In Mie theory the scattering (Q_{sca}) and absorption (Q_{abs}) cross sections are defined as the effective area over which the particle absorbs or scatters light. The sum of these

two processes is termed extinction (Q_{ext}) and characterizes the total loss that the incident radiation undergoes.

Calculated by solving Maxwell's equations and using a series expansion of spherical harmonic wave equations, Mie theory presents an analytic solution composed of multipolar modes with order l , from the lowest dipole order ($l = 1$) through quadrupolar modes ($l = 2$) to higher order multimodes. For a particle of radius a , frequency dependent permittivity $\epsilon_p(\omega)$ and permeability $\mu_p(\omega)$ embedded in a medium of ϵ_m, μ_m and interacting with incident light of wavelength λ_0 , the expressions for the scattering and extinction cross sections are [11, 12]:

$$Q_{sca} = \frac{2\pi}{k^2} \sum_{l=1}^{\infty} (2l+1) (|a_l^2| + |b_l^2|) \quad (2.4)$$

$$Q_{ext} = \frac{2\pi}{k^2} \sum_{l=1}^{\infty} (2l+1) \text{Re}[a_l + b_l], \quad (2.5)$$

where $k = \frac{\omega}{c} n_m = \frac{2\pi}{\lambda_0} n_m$ and c the speed of light. The absorption cross section is obtained by the subtraction of the extinction and scattering cross sections $Q_{abs} = Q_{ext} - Q_{sca}$. The Mie coefficients of the scattered field, a_l and b_l , represent the electric and magnetic partial waves, respectively (see figure (2.1)), and can be defined using the spherical Bessel functions:

$$a_l = \frac{\mu_m m^2 j_l(mx) [x j_l(x)]' - \mu_p j_l(x) [mx j_l(mx)]'}{\mu_m m^2 j_l(mx) [x h_l^{(1)}(x)]' - \mu_p h_l^{(1)}(x) [mx j_l(mx)]'} \quad (2.6)$$

$$b_l = \frac{\mu_p j_l(mx) [x j_l(x)]' - \mu_m j_l(x) [mx j_l(mx)]'}{\mu_p j_l(mx) [x h_l^{(1)}(x)]' - \mu_m h_l^{(1)}(x) [mx j_l(mx)]'}, \quad (2.7)$$

where j_l and y_l are the first and second kind spherical Bessel functions, respectively, $h_l^{(1)}(x) = j_l(x) + iy_l(x)$ the Hankel function of the first kind, $x = ka$ the *size parameter*, and $m = \frac{n_p}{n_m}$ is the relative refractive index.

When either denominator of the Mie coefficients in equations (2.6, 2.7) approaches zero, the corresponding l 'th normal mode will dominate in the series expansion of the scattered field. As a result we can characterize a set of *morphological dependent resonances* (MDR), of a given dielectric sphere, by discrete values of the size parameter (x). Accordingly, this defines a set of complex frequencies that correspond to the l 'th electric or magnetic "natural mode" of the given particle. The real part of the complex frequencies are close to the resonant frequency ω_r , while the imaginary parts determine the resonance linewidths Γ .

A relatively similar analytical treatment can be done to a few more morphologies such as a coated spheres, and infinitely long circular cylinders. For a chosen morphology, a

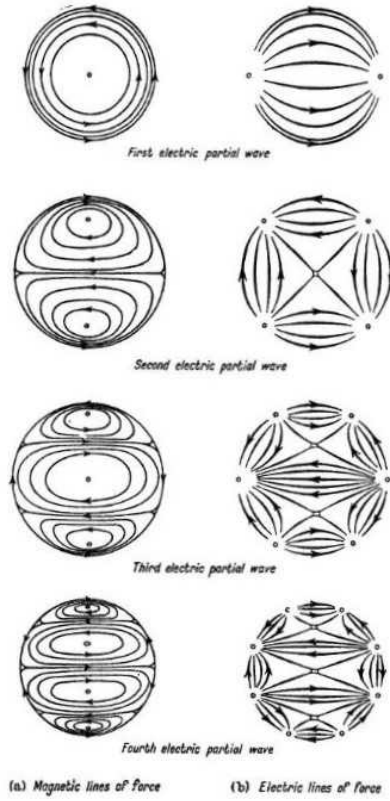


Figure 2.1: Lines of force of the first four electric and magnetic partial waves [1].

particle acts as a resonator for the incident wave that circumnavigates it after either penetrating inside, remaining confined by total internal reflection, or propagating as a wave attached to its outer surface and being evanescent away from it. In both cases the field is described by surface waves interfering with themselves after traveling around the particle's perimeter a number of cycles, thus returning to the starting position in phase. The described mechanism results in large cross sections as well as strong localized near fields, at the mentioned size parameters or "natural frequencies", due to the enhancement of the l 'th mode in the Mie series.

The "natural modes" can be considered as virtual modes due to their radiative nature for any real "natural frequency" ω_r , but due to the imaginary part of the frequency Γ , the absorption of energy is lost through dissipation. We can define a quality factor (Q – factor) as $2\pi \times \text{energy stored in the particle} / \text{dissipated energy per cycle}$, that is:

$$Q - \text{factor} = \frac{\omega_r}{\Gamma}. \quad (2.8)$$

Since the time period of the resonant process is $\tau = 1/\Gamma$, the Q-factor provides information

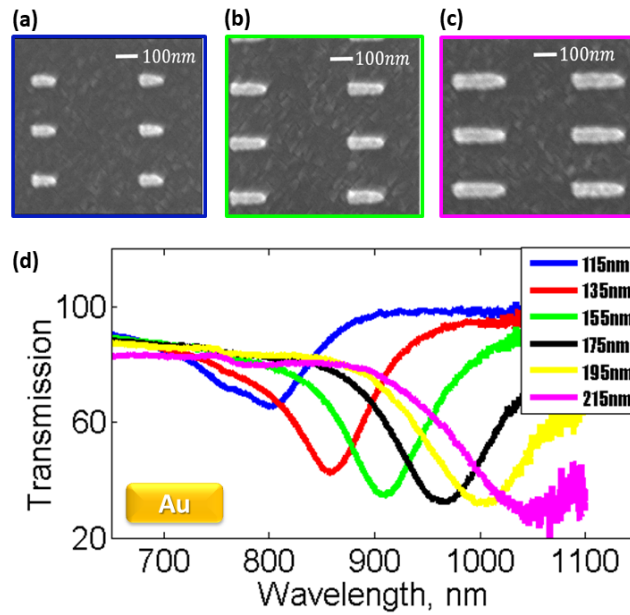


Figure 2.2: Plasmonic response of metallic nano-bars. (a)-(c), SEM images of gold nano-bars of different lengths, 115nm, 155nm and 215nm, respectively. (d) Transmission spectrum of the LSPR absorption lines for varying lengths of gold nano-bars. Figures (a)-(d) were borrowed with consent from the work of a colleague from my lab.

about the temporal length of the process.

Each l 'th normal mode is generally composed of one electric and one magnetic partial wave. For most examples investigated until today the electric partial wave was the dominating factor of the resonance ($b_l \ll a_l$). However, in recent years, strong magnetic coefficients b_l were found in high refractive index particles, constituting a novel research line of optics, which is at the heart of the design of resonant dielectric metamaterials and metasurfaces.

2.2.1 Localized surface plasmon resonance

When dealing with conductors, usually novel metals, MDRs are modeled as plasma oscillations of the free electron cloud, induced by the incident light wave, thus emitting an electromagnetic field which, like a surface plasmon-polariton, is evanescent away from the particle surface. Since this phenomenon is highly localized with respect to the wavelength it has been given the name *localized surface plasmon resonance (LSPR)*.

Figure (2.2) presents a transmission spectrum of Gold nano-rods in varying lengths

as well as a few *scanning electron microscope* (SEM) images. When incident light, polarized with the long axes of the rod, penetrates the particle, it excites an electric dipole mode LSPR, forming a Lorentzian shaped absorption/transmission line. By increasing the particle size, the real value of the resonant frequency ω_r undergoes a red-shift into the NIR spectrum. A similar observation regarding the increasing imaginary part Γ , due to the increase in electron-electron interactions, is illustrated by the widening of the Lorentzian shaped line. This points out the increase in dissipative energy loss as the excitation energy is decreased.

2.2.2 *Whispering gallery modes*

High refractive index dielectric particles, such as semiconductors, also act as MDRs. The field enhanced inside the particle tends to be confined close to the particle surface as the l 'th order increases. As implied, *whispering gallery modes* (WGM), borrowed from the field of acoustics, where termed by Lord Rayleigh by his explanation for sound waves propagating around the circular gallery of St Paul's cathedral. WGMs are well described as surface waves propagating along concave surfaces and are usually an attribute to the higher confined l 'th order modes in dielectric particles.

The mathematical structure of either modes, LSPR's, WGM's or what remains in between, behave similarly to atomic orbitals, such that grouping particles close together, in pairs or even larger groups, can result in similar dynamics to the coupling of atoms into molecules. The outcome of such a coupling process can be manifested in the splitting of the single particle resonance. As an example, when placing two perpendicular gold nano-bars with a small gap between their edges we create an effective two level system as seen in figure (2.3). By exciting the nano-bars with an incident electromagnetic wave, we no longer receive a Lorentzian line shaped resonant peak corresponding to the electric dipole (a_1) natural mode (as seen in figure (2.2)), but instead we receive the splitting into two separate shifted resonant peaks corresponding to the emergence of symmetric and anti-symmetric modes. Figure (2.3) shows the periodic energy transition between the two perpendicular bars plotted as a function of time. The time period of roughly $\tau \approx 15 fs$ suggests this process is lossy and has a relatively low Q-factor of ~ 5 (see eq.2.8) as expected from a plasmonic process.

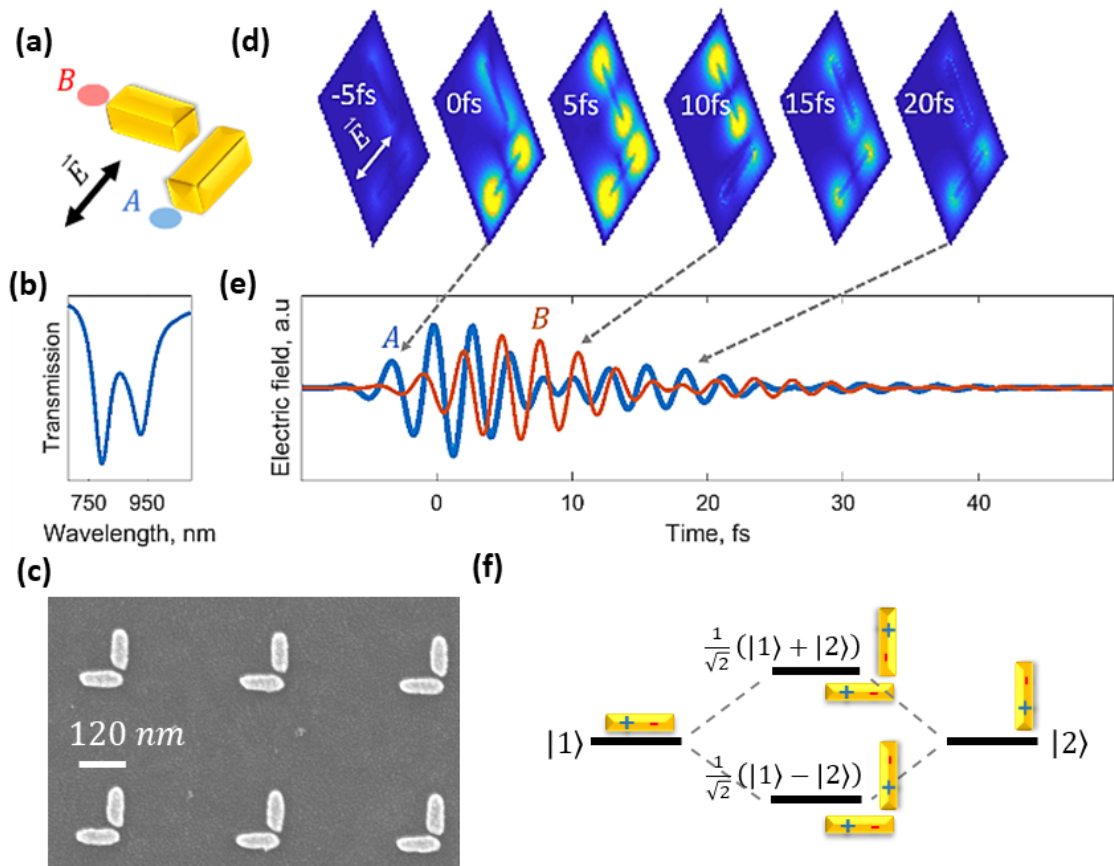


Figure 2.3: The coupling between two perpendicular nano-bars. (a) View of the spatial arrangement of two gold nano-bars and the polarization of the incident light wave. (b) Transmission spectrum that exhibits the splitting of the single LSPR electric dipole resonance into two shifted resonant lines. (c) SEM image of a fabricated array of the pair coupled particles. (d) Simulation snapshots presenting the spatial distribution of the localized electric field intensity in different time constants. (e) Electric field intensity plots as a function of time for monitors placed in points A (blue) and B (red), see points in (a). (f) A schematic energy level diagram describing the splitting process due to the emergence of a symmetric and anti-symmetric state. Figures (a)-(e) were borrowed with consent from the work of a colleague from my lab.

2.3 Characterizing a metasurface

As stated before, metamaterials are engineered to achieve some desirable bulk behaviour by arranging scatterers in a pattern throughout three dimensional space. The most convenient method by which to model metamaterials is effective medium theory. This approach enables to extract the effective permittivity and permeability by the averaging of electric and magnetic fields over a given period cell composing the metamaterial (the averaging is valid only for wavelengths large compared to the unit cell). Empirically, using the Nicolson-Ross-Weir approach (or its modified version for double negative materials), the extraction of the effective parameters is enabled by obtaining the reflection and transmission properties of the material.

When reducing to a two-dimensional description, we are in fact considering a metasurface that consists of a single unit cell in the axis vertical to the surface. Attempts to use a similar bulk parameter analysis on metasurfaces was less successful. The difficulty arises from the need to define an arbitrary non-zero thickness to the metasurface in order to calculate the effective permittivity and permeability. This thickness was originally (in three dimensions) consider as the vertical unit cell length, but since this cell does not have any neighbouring cell, the surface thickness cannot be defined uniquely. Assigning different thicknesses to the classical algorithms for bulk parameter extraction give results that depend on sample size, i.e non uniquely defined parameters as seen in figure (2.4). It is important to state that the effective bulk properties of a metasurface extracted this way can have non-physical behaviors as well. For example, causality (as manifested in the Kramers-Kronig relations) may be violated, or a passive material may exhibit bulk permittivity or permeability with gain.

The correct way suggested for modeling the phase shift and possibly a change in amplitude is through applying generalized sheet transition conditions for an infinitely thin sheet [2, 13]. They allow surface distribution of scatterers to be replaced with a boundary condition that is applied across an infinitely thin equivalent surface. The size and shape characteristics of the scatterers are incorporated into this boundary condition through the surface susceptibilities (surface polarizability densities). Since this topic is not at the heart of the thesis I will not present the uniquely characterizing retrieval technique for determining the surface susceptibility dyadics of a metasurface.

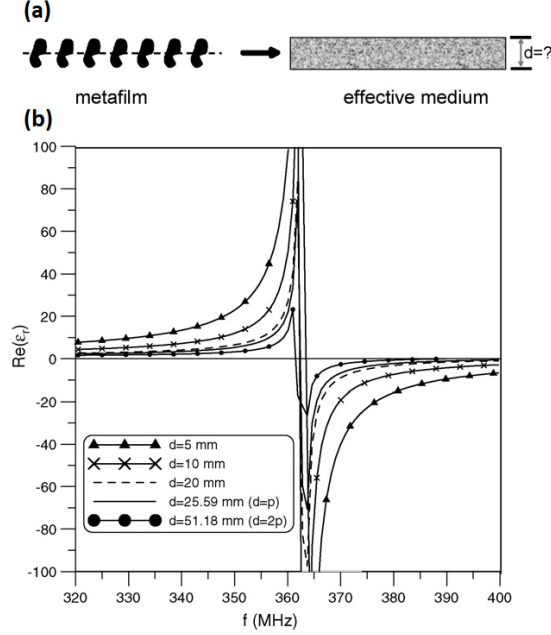


Figure 2.4: (a) Representing a metamaterial as an effective medium of thickness d . (b) The effective permittivity of a metasurface modeled as an effective medium for different layer thicknesses d (spherical particles with radius of 10 mm, spacing of 25.59 mm, $\epsilon = 2$, and $\mu = 900$ - modeled for radio frequency) [2].

2.4 Interference between Mie resonances and directional scattering

During the early years of the 17th century it was found that resonances - such as mechanical, acoustic and electromagnetic ones - are a universal characteristic of many physical systems. The spectral dependence of these resonances is generally described by the Lorentzian formula, with dynamical variables arising from a simple linear differential equation. For many years, the Lorentzian formula was regarded as the fundamental line-shape of a resonance [3].

2.4.1 Fano resonance

In 1961, during a quantum mechanical study of the autoionizing states of atoms [14], Ugo Fano discovered a new type of resonance that now bears his name. In contrast to a Lorentzian resonance, the Fano resonance exhibits a distinctly asymmetric shape with the following functional form:

$$I \propto \frac{(F\Gamma + \omega - \omega_r)^2}{(\omega - \omega_r)^2 + \Gamma^2}, \quad (2.9)$$

where ω_r and Γ are standard parameters that denote the position and width of the resonance, respectively and F is the so-called Fano parameter, which describes the degree of asymmetry. The microscopic origin of the Fano resonance arises from the constructive and destructive interference of a narrow discrete resonance with a broader one. The Fano resonance has generally been regarded as a feature entirely specific to quantum systems. However, wavefunction interference phenomena are also ubiquitous in classical optics and have been observed for example in Wood anomalies of diffraction gratings. Due to ohmic losses the observation of Fano resonances in plasmonic particles is considered difficult, but their appearance in Mie scattering of high index dielectric particles owing to interference between a narrow electric (or magnetic) quadrupole peak and a broad electric (or magnetic) line-shape, for instance, are observed frequently (see figure (2.5)).

In section 2.2 we defined the single spherical particle total scattering and extinction cross sections (eq. 2.4, 2.5) which are proportional to the sum of intensities and hence insensitive to interference effects. Fano resonance requires an observable which is sensitive to these effects and therefore we must look for a differential scattering spectra observable such as *radar back scattering* (RBS) and *forward scattering* (FS) cross sections which are defined as follows [10]:

$$Q_{RBS}^{(sca)} = \frac{1}{(ka)^2} \left| \sum_{l=1}^{\infty} (2l+1) (-1)^l (a_l - b_l) \right|^2, \quad (2.10)$$

$$Q_{FS}^{(sca)} = \frac{1}{(ka)^2} \left| \sum_{l=1}^{\infty} (2l+1) (a_l + b_l) \right|^2. \quad (2.11)$$

For a plasmonic sphere, as illustrated in figure (2.5), we see a wide symmetric line-shaped electric dipole (a_1) resonance and a narrow asymmetric electric quadrupole (a_2) Fano-resonance due to the electric dipole-quadrupole interference. Interesting enough, the angular distribution of scattered field intensity at frequencies near the Fano-resonance exhibit strong variations in between forward and backward scattering. This observation gives a hint to the important role of directional scattering in metasurfaces [10].

2.5 Electromagnetically induced transparency

EIT is a technique for eliminating the effect of a medium on a propagating beam of electromagnetic radiation [15], i.e taking an otherwise opaque medium and opening a frequency dependent "transparency window" through it. Taken from the field of atomic physics, this

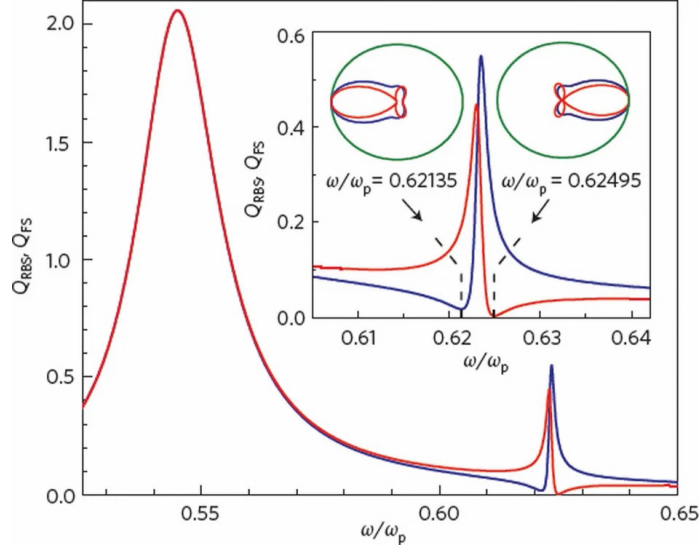


Figure 2.5: RBS (red) and FS (blue) cross-sections versus normalized frequency ω/ω_p . The dielectric permittivity ϵ is described by the Drude formula for a plasmonic sphere. The calculations follow equations 2.10, 2.11 for a_1 and a_2 only. Inset shows polar scattering diagrams in the $x - z$ plane near the quadrupole resonance of a plasmonic particle. Red lines represent linearly polarized light; blue lines represent non-polarized light [3].

phenomenon requires a three level system in which the transition from $|1\rangle \rightarrow |2\rangle$ is considered a Raman (non-allowed) transition. If we assume the following Hamiltonian for the system [4]:

$$\hat{\mathcal{H}} = \hat{\mathcal{H}}_0 + \hat{\mathcal{H}}_1 = \begin{pmatrix} \hbar\omega_1 & 0 & 0 \\ 0 & \hbar\omega_2 & 0 \\ 0 & 0 & \hbar\omega_3 \end{pmatrix} - E \begin{pmatrix} 0 & 0 & \wp_{13} \\ 0 & 0 & \wp_{23} \\ \wp_{31} & \wp_{32} & 0 \end{pmatrix}, \quad (2.12)$$

where $\hat{\mathcal{H}}_0$ and $\hat{\mathcal{H}}_1$ are the bare atom and interaction Hamiltonians respectively, $\hbar\omega_i$ is the i 'th energy level, $E = \mathcal{E}_p \cos \omega_p t + \mathcal{E}_c \cos \omega_c t$ the electric field consisting of the pump \mathcal{E}_p and coupling \mathcal{E}_c amplitudes, with frequencies ω_p and ω_c . $\wp_{ij} = \langle i | q\mathbf{d} | j \rangle$ is the dipole element between states $|i\rangle$ and $|j\rangle$. Notice that $\wp_{12} = 0$ represents a forbidden transition as defined earlier. Since the Mathematical treatment for analyzing the EIT eigen-value problem is quite long, and less relevant for this thesis, I will only show the conditions for which the 3-level system satisfies the EIT phenomenon. After applying the rotating wave approximation and moving to the time and phase independent frame on equation 2.12, we are left with the following Hamiltonian:

$$\hat{\mathcal{H}} = \frac{\hbar}{2} \begin{pmatrix} 0 & 0 & -\Omega_p \\ 0 & 2(\Delta_p - \Delta_c) & -\Omega_c \\ -\Omega_p & -\Omega_c & 2\Delta_p \end{pmatrix}. \quad (2.13)$$

Here $\Omega_p = \frac{e_p |\mathcal{P}_{13}|}{\hbar}$ and $\Omega_c = \frac{e_c |\mathcal{P}_{23}|}{\hbar}$ are the pump and coupling Rabi frequencies, and Δ_p and Δ_c stand for the detuning as illustrated in figure (2.6). Approximating $\Delta_p \approx \Delta_c \equiv \Delta$

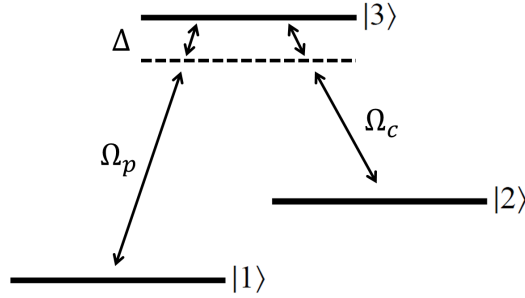


Figure 2.6: Schematic illustration of a three-level system. $|1\rangle$ signifies the ground state, $|3\rangle$ the "bright" state and $|2\rangle$ the "dark" state. Ω_p donates the Rabi frequency used to probe the "bright" state from the ground state, and Ω_c the coupling Rabi frequency between the "bright" state and the "dark" state. $\Delta = \Delta_p = \Delta_c$ signify the equal detuning in the EIT case.

and also assuming $\Omega_p \ll \Omega_c$, i.e the coupling $|3\rangle \rightarrow |2\rangle$ is a lot stronger than $|1\rangle \rightarrow |3\rangle$, results in an EIT spectrum, as plotted in figure 2.7.

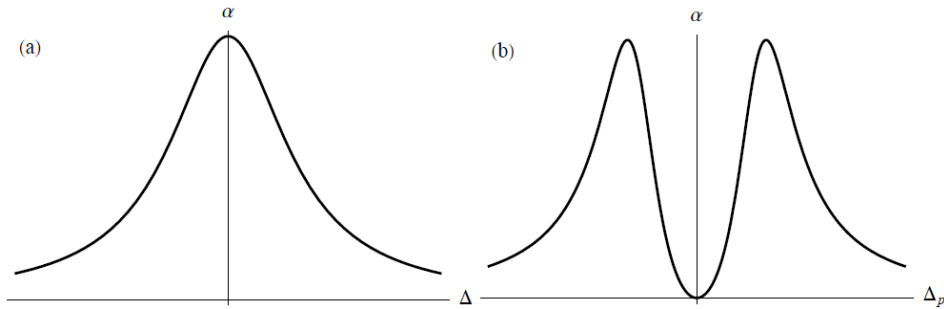


Figure 2.7: (a) A typical absorption (α) spectrum ,and (b) an EIT absorption spectrum. In both cases, Δ is the detuning from resonance. The subscript p in (b) signifies that the probe frequency is being scanned [4].

The quantum mechanical mechanisms underlying EIT are quite complicated and not easily intuited. One simple way to think of EIT is as a result of destructive interference between transition probabilities. Given the three-level structure, there exist two paths

between state $|1\rangle$ and state $|3\rangle$: $|1\rangle \rightarrow |3\rangle$ and $|1\rangle \rightarrow |3\rangle \rightarrow |2\rangle \rightarrow |3\rangle$. If, for a given frequency, the probabilities of each of these transitions occurring in the system have opposing phases, destructive interference could occur and result in no transitions from $|1\rangle \rightarrow |3\rangle$. This would, in turn, lead to a reduction in the absorption of the field resonant with that transition.

When adding to the spatial arrangement of figure (2.3.a) a third Bar as seen in figure (2.8), apart from the "bright" radiating dipole excitation (which we will refer to as state $|3\rangle$), another "dark" non radiating quadrupolar mode is excited (state $|2\rangle$). The coupling between the two excited modes, while including a non excited ground state $|1\rangle$, leads to a three level system as illustrated in figure (2.6) with resulting spectrum analogue to the so called EIT phenomenon. This was the pioneering work by S. Zhang *et al.* [5], published in 2008, followed by others, who adopted the analogy of EIT to metasurfaces [16, 17, 18, 19, 20, 21].

In the presented analogy a narrow frequency band propagates freely through the material but undergoes extreme dispersion. One specific length parameter d , the gap width in figure (2.8.a), dictates the coupling strength between the "bright" mode and the "dark" mode ($d \Rightarrow \phi_{23}$). When the coupling is strong ($d = 40nm$ plot in figure (2.8.b)), destructive interference between the two transitions eliminates the influence of the medium. It is interesting to see how small delicate changes in d modify the transmission/absorption spectrum (proportional to $Re(E)/Im(E)$ respectively).

Due to the extreme dispersion, the "transparency window" accumulates a large linear phase which leads to a group delay $\tau_\omega = \frac{d\Phi_\omega}{d\omega}$ resulting in "slow light".

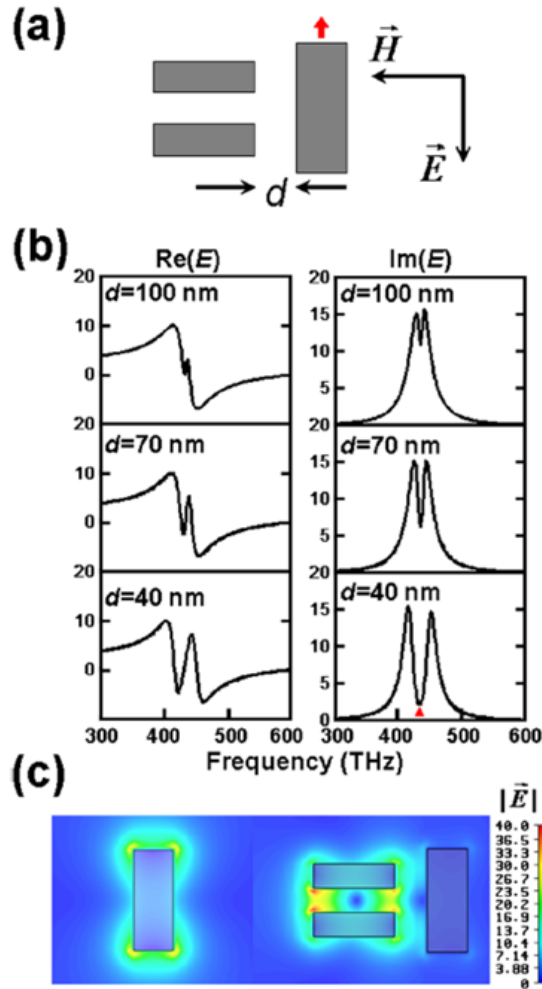


Figure 2.8: Plasmonic induced transparency (EIT analogue). (a) Top view of the plasmonic system consisting of a radiative element and a dark element with a separation distance d , with light incident at the normal direction. (b) The real and imaginary parts of a \vec{E} probe placed 10nm from the end facet of the radiative antenna (red arrow in (a)) for separations ranging from $d = 40$ to 100nm between the radiative and dark elements. (c) The 2D field intensity plot of an uncoupled radiative atom (left) and a radiative atom coupled with a dark atom with a separation of 40nm (right) at a frequency of 428.4THz , as indicated by the red triangle in (b) [5].

3 Motivation - Dielectric metasurfaces in the mid IR

Resonances in metasurfaces play a major role in the nanophotonics research. Yet the majority of metasurface resonant mechanisms are absorptive in their nature thus very lossy, with extremely low Q factors. My aim in this thesis was to find the right method for creation of high Q-factor resonant metasurfaces in the MIR.

Such advance will be naturally integrated with the three cornerstones of our "Femto-Nano Laboratory": 1. MIR broadband, 2 – $5\mu m$, ultra-short source which building is in progress. 2. Ultra fast dynamics research utilising our femto-second lasers for pump-probe experiments. 3. Near field measurements using the *Near-field scanning optical microscopy* (NSOM) system for measuring evanescent field distribution in the nano-scale.

3.1 Why Dielectric meta surfaces

One route to pursue this goal was through the design of plasmonic metasurfaces with resonant frequencies in the MIR. There are two ways to shift the plasmonic resonance to the MIR:

The first is by adjusting the MDR of a noble metal particle to excite a LSPR with MIR wavelengths. According to the Drude model, both real and imaginary parts of the permittivity ϵ , plotted in figure (3.1.a), increase dramatically in their absolute value with wavelength. Due to the correlation between the two components of ϵ and the extinction cross section, such an MDR will have a poor Q-factor in the mid-IR optical range, or in other words undergo significant scattering and ohmic losses.

The second and relatively novel route is by blue-shifting the plasma frequency of semiconductors through the injection of free-carriers, i.e producing nano-particles of heavily doped semiconductors. The advantage of such an approach is manifested in the ability to

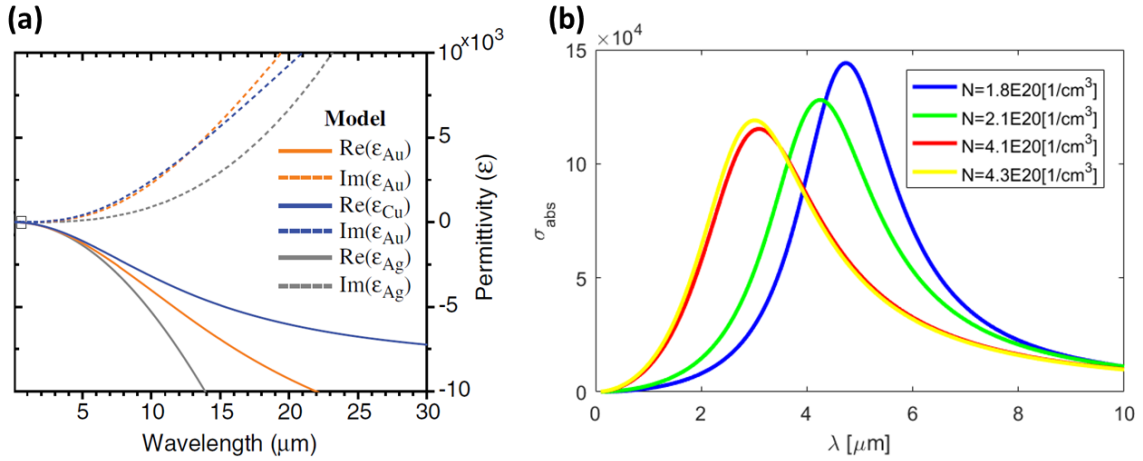


Figure 3.1: Two routes for MIR plasmonics: (a) Drude model of real (solid) and imaginary (dashed) permittivity for the three noble metals: Gold (Au), Copper (Cu) and Silver (Ag) [6]. (b) Absorption cross-section simulation of a Boron-type Heavily doped Si particle, with carrier concentrations (N) of over $10^{20}[\text{cm}^{-3}]$, geometrical aspect ratio of $1/2$.

accurately control the doping concentration and by that control the plasma frequency and inter-band absorption. Following a short study, we saw that this route also leads to high absorbent resonances as reflected from figure (3.1.b). Increase in carrier density means the increase of defects and subsequently the decrease in mobility, which results in loss.

After further investigation it became obvious that high absorbent wide resonances are less suitable for our source and measurement capabilities. Furthermore, low Q-factor resonances are not suitable for pump-probe experiments, since the shift in resonance would be very difficult to identify. In the pursue for a suitable solution, I was exposed to the field of all-dielectric metamaterials. As mentioned in the introduction (chapter 1), since dielectric resonators undergo negligible absorption, they can be easily utilized to create high Q-factor resonances. In contrast to plasmonic particles which are mainly limited to electric multipolar resonances, in all-dielectric metasurfaces it is possible to excite both electric and magnetic multipolar modes. The "natural modes" of the system are doubled, and give place to a broad range of new resonant effects associated with interference of electric and magnetic multipoles.

4 Experimental realization

In this section, I will cover my main project on measuring the optical characteristics of Silicon-based metasurfaces. First, I will explain the considerations for choosing the constituent materials, then I will focus on the characteristics of the samples I designed through FDTD simulations. I will explain the fabrication process and detail some of the challenges I have faced. Finally I will finish with my measurement apparatus and results.

4.1 *Choosing the constituent materials*

Silicon is a highly attractive material, due to its wide availability, low cost, and mature fabrication technology. The vast majority of resonant dielectric nano-phonic structures so far have relied on Silicon as the constituent material. The optical properties of Silicon are almost ideal for a strong Mie-resonant response in a wide spectral range [22]: Silicon has a high refractive index of 3.5 ($\epsilon \sim 12$) and negligible absorption losses from the telecom spectral range and further to the MIR, as required for a significant magnetic dipolar response. Only for wavelengths below $1.1\mu m$, the electronic bandgap of Silicon marks the onset of absorption. Due to the indirect nature of the electronic bandgap, absorption remains relatively low for wavelengths exceeding 500nm, allowing for the observation of strong Mie-type resonances in Silicon nano-particles throughout the visible spectral range [23]. At the same time, Silicon nano-structures are immediately CMOS-compatible and suitable for on-chip photonic architectures, making them highly integrable for electronic applications.

In addition to their good optical properties, Silicon nano-structures are mechanically and thermally quite robust. Another intriguing aspect is the native layer of 3nm SiO_2 , which forms at the surface of Silicon under ambient conditions. This layer renders Silicon nano-structures a convenient platform for chemical surface functionalization, making it an accessible platform for bio-sensing or hybridization with other functional materials.

Generally, Silicon can be used in its various forms, monocrystalline, polycrystalline, and amorphous, providing another degree of freedom for tailoring linear and nonlinear optical response through the properties of the constituent material while preserving the advantages of using a Silicon platform.

For my project I chose to order a 230nm monocrystalline Silicon thin layer grown over a Sapphire substrate. The Sapphire (Al_2O_3) substrate with refractive index of roughly 1.7 is completely transparent in the visible wavelengths (essential for transmission imaging) but starts to drop off at wavelengths greater than approximately $4.5\mu m$, which suits a satisfying range of my spectral area of interest. Moreover, in terms of the fabrication process, on which I will elaborate on more in section 4.3, monocrystalline Silicon is more suitable in means of carving sharp detailed morphologies during the etching processes from a uniform Silicon layer to the designated metasurface. On the contrary, the sapphire substrate is nearly insensitive to the ion etching process needed for monocrystalline Silicon and hence functions as an effective stop layer.

4.2 FDTD Simulations

Since, only a few simple isolated particle morphologies are analytically solvable via Mie theory, when dealing with more complex morphological designs which can include interaction between subwavelength building blocks, we must introduce numerical methods. Finite difference time domain (FDTD) simulations are the gold standard for numerical modeling of nano-phonic devices. I used for this project the *Lumerical software* which utilizes computer aided design (CAD) to solve Maxwell's equations in space and time for a given 3D design.

The EIT analogue design consists of an array of discs and bars arranged alternately in a 2D square lattice with unit cell dimensions of $1280 \times 1280nm$ as seen in figure (4.1). Prior to simulating an EIT analogue design, I would like to first analyze separately its building blocks.

4.2.1 Bar and disc arrays

When simulating the same unit cell size as in figure (4.1) which consists only a disc or alternatively only a bar (without changing their size) we receive an overlapping broadband dipole excitation as seen in the reflection spectrum presented in figure (4.2). Varying the metasurface's geometry, i.e varying the lattice constant in the disc or bar lattice, results

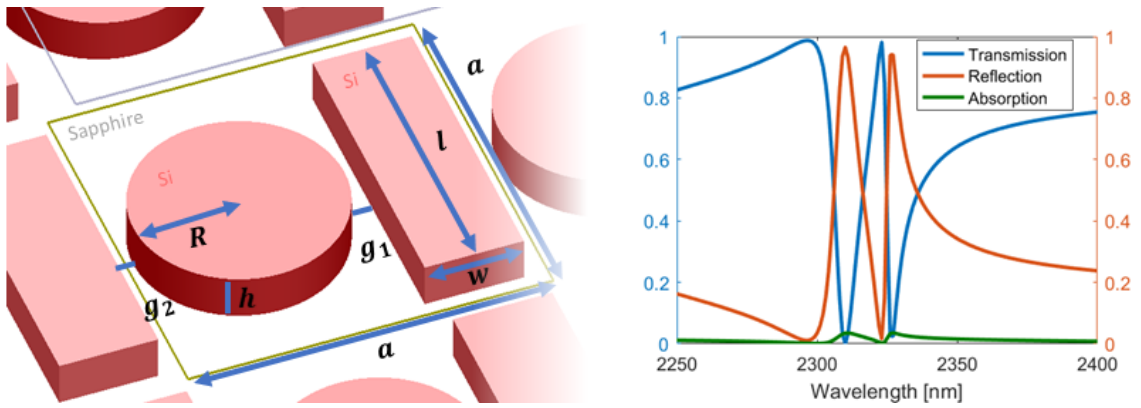


Figure 4.1: Left: Silicon (red) on Sapphire EIT analogue metasurface design. $a = 1280nm$, $h = 230nm$, $l = 1022nm$, $w = 347nm$, $R = 369nm$, $g_1 = 85.5nm$, $g_2 = 109.5nm$. The detuning $\Delta = g_2 - g_1$ is the parameter that links the geometry with the coupling strength between the "bright mode" and the "dark mode". **Right: Simulation of the resulting EIT transmission, reflection and absorption spectrums.** You can clearly see the negligible absorption of this process.

with a dramatic shift in transmission/reflection spectrums as seen in figure (4.3). From figure (4.3) it becomes clear that the interaction length (cell size) between the lattice's building blocks impacts markedly the interference effects between the excited natural modes of the metasurface.

When arranging the discs and bars alternately (as illustrated in figure (4.1)) with symmetric gaps between every disc to its two adjacent bars ($g_1 = g_2 = 97.5nm$) we receive a single Fano-resonance peak centered at $\lambda_r = 2315nm$, as seen in figure (4.4.a). The Fano-resonance is the expected response of an interferences between a broad and narrow reso-

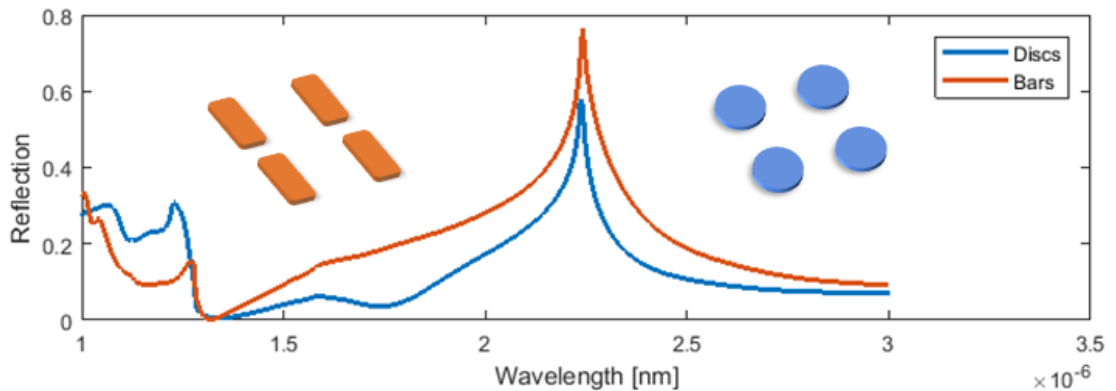


Figure 4.2: Reflection spectrum (normalized units) of separated bar (orange) and Disc (blue) square lattices with a lattice constant of $1280nm$.

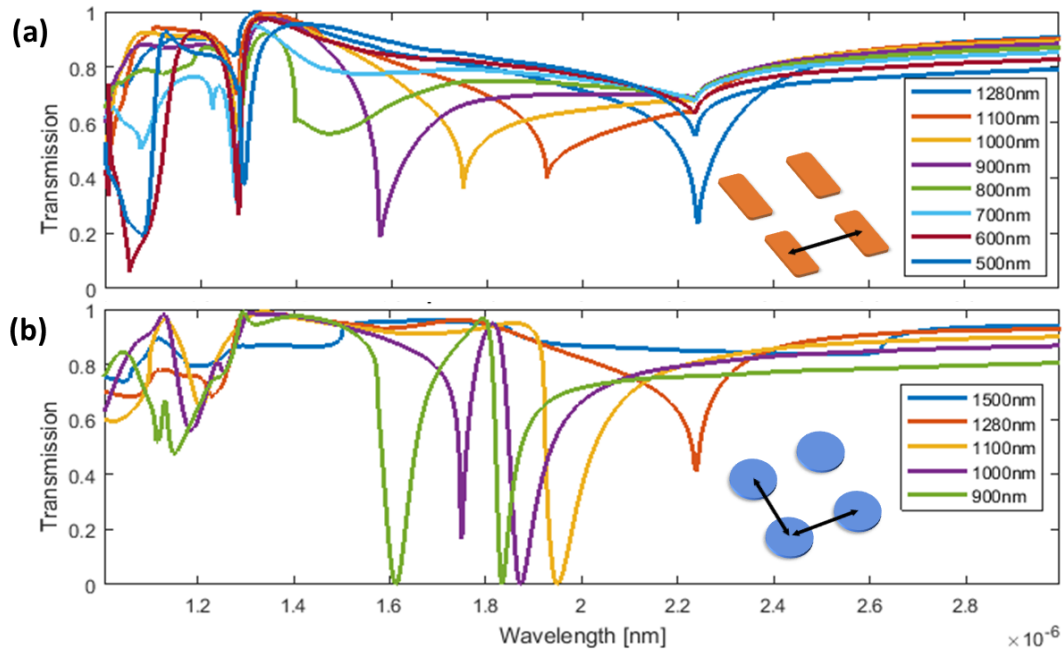


Figure 4.3: Simulated transmission spectrum for varying lattice constants. (a) Bar lattice with a varying horizontal lattice constant. Bar length $1022nm$, width $347nm$ and height $230nm$. The vertical lattice constant for all simulations is $1280nm$. The dipole moment centered at $2250nm$ (for lattice constant $1280nm$) is blue shifted with varying amplitude as the lattice constant shortens. In addition as the lattice constant shortens other high order resonances appear. (b) Disc lattice with a varying lattice constant (vertical and horizontal). Disc radius $400nm$ and height $230nm$. The dipole moment centered at $2250nm$ (for lattice constant $1280nm$) is blue shifted and enhanced as the lattice constant shortens. In addition a magnetic dipole resonance appears.

nance as mentioned in section 2.4.1. The excitation energy is well below the Si bandgap (see section 4.1) and further lower than the two-photon absorption threshold. In this case the Fano-resonance arises from the interference of the two electric dipole excitations. The first dipole is excited collectively among the discs and dominates in lower wavelengths (with respect to λ_r , see figure (4.4.b-d)), while the second dipole is excited, with opposite phase, among the bars and seems to be narrow compared to the previous. Around λ_r , both resonances interfere resulting in highly directional forward and backward scattering.

4.2.2 Electromagnetic induced transparency analogue

In order to create an EIT analogue system through Fano-type interference we must excite a "dark" mode, inaccessible from free space, with a strong coupling coefficient to an accessible "bright" mode. If these two resonances are brought in close proximity in both the

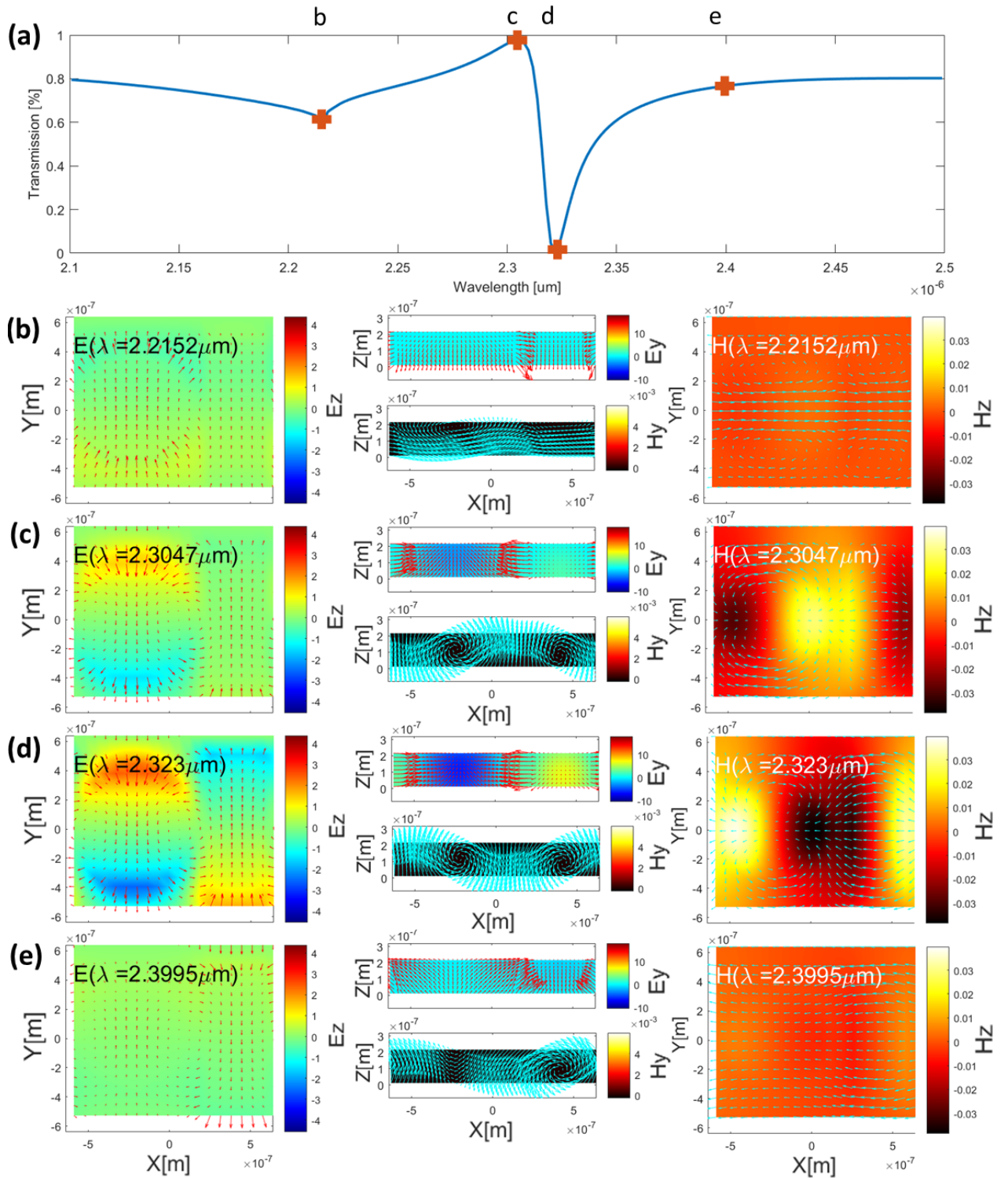


Figure 4.4: Near field profile analysis of the symmetric geometry arrangement ($\Delta = 0 \text{ nm}$). (a) Transmission line (blue), and brown marks that specify the 4 wavelength chosen for field profile display. (b-e) Left: Electric field x-y profile positioned in $z = 50 \text{ nm}$. The colorbar indicates $\Re(E_z)$ and red arrows $\Re(E_x, E_y)$. Right: Magnetic field x-y profile positioned in $z = 125 \text{ nm}$. The colorbar indicates $\Re(H_z)$ and red arrows $\Re(H_x, H_y)$. Middle: In every row the upper display is the electric field x-z profile, and lower display the magnetic field x-z profile, both positioned in $y = 0$. The profiles include a caption specifying their excitation wavelength.

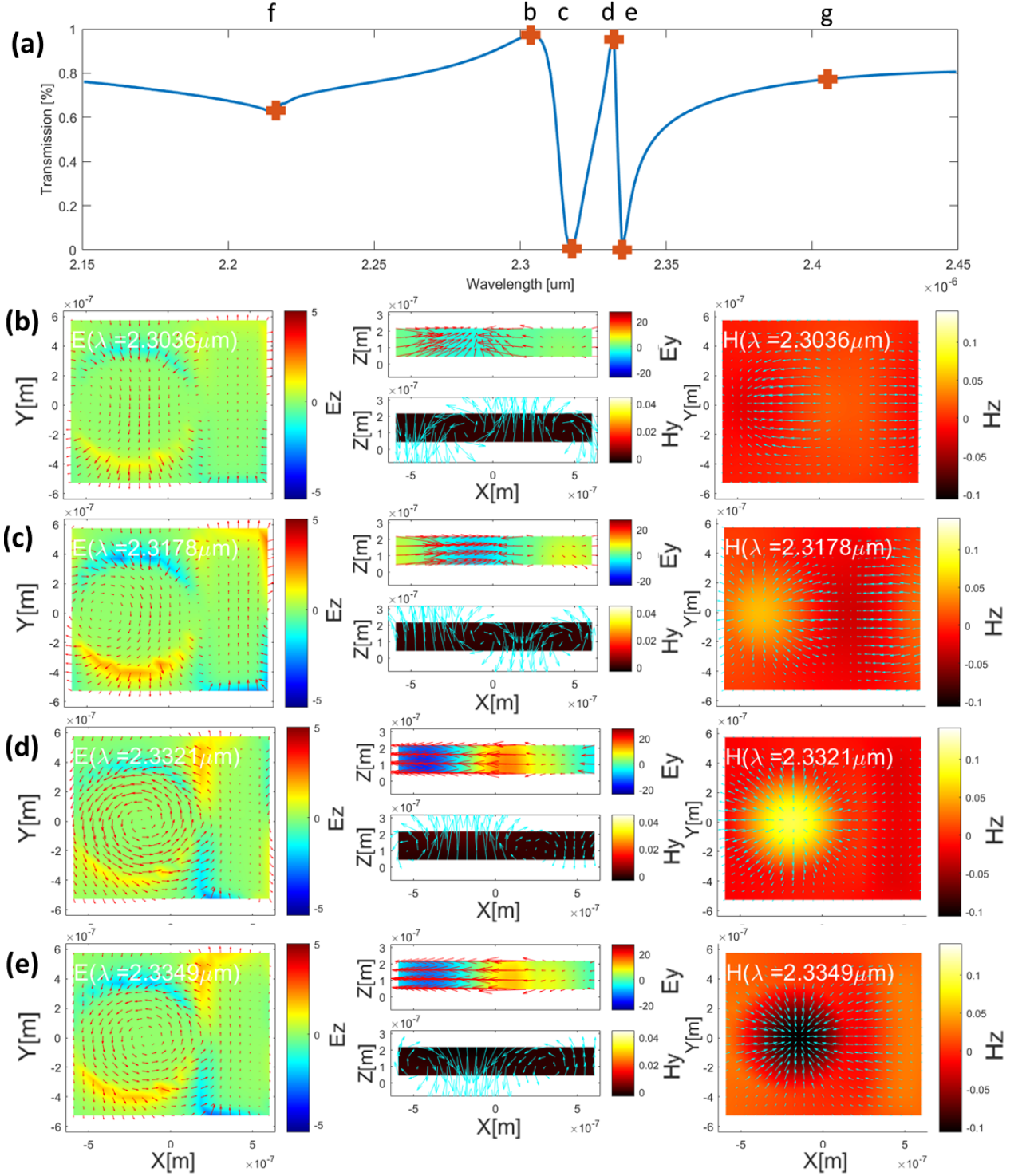


Figure 4.5: Near field profile analysis of the EIT analogue, asymmetric geometry arrangement ($\Delta = 24nm$).(a) Transmission line (blue), and brown marks that specify the 6 wavelength chosen for field profile display. (b-e) Left: Electric field profile in $z = 218nm$, colormap indicates $\Re(E_z)$ and red arrows $\Re(E_x, E_y)$. Right: Magnetic field profile in $z = 218nm$, colormap indicates $\Re(H_z)$ and blue arrows $\Re(H_x, H_y)$. Middle: Upper display is the electric field profile, and lower display the magnetic field profile in $y = 0$. The profiles include a caption specifying their excitation wavelength. Points (f)-(g) display profiles similar to the same wavelengths in figure (4.4.b,e).

spatial and frequency domains, a narrow transmission window is formed. As we have seen from the symmetric arrangement (figure (4.4)) a Fano-type "bright mode" is excited due to the dipole excitation of the bars and discs. In order to excite a non-radiating "dark mode" we must break the symmetrical arrangement of the building blocks (the symmetry causes perfect destructive interference between two magnetic forces). One effective way to do so is by collectively shifting the disc location towards one of the adjacent bars, and thereby excite a magnetic dipole "dark mode" oriented perpendicular to the metasurface.

Figure (4.5) shows the EIT analogue spectrum together with 2D field profiles for 4 different excitation wavelengths. While wavelength points (f), and (g) are not displayed since they show an electric dipole excitation similar to the field profiles in figure (4.4.b, e) of the symmetric case, profiles (4.5.b-e) display a magnetic dipole "dark" mode arising perpendicular to the disc center and interfering with the electric dipoles. The magnetic dipole is excited due to the detuning in the interference of two opposite magnetic forces, as illustrated in figure (4.6). Both radiative and non-radiative damping are minimized through

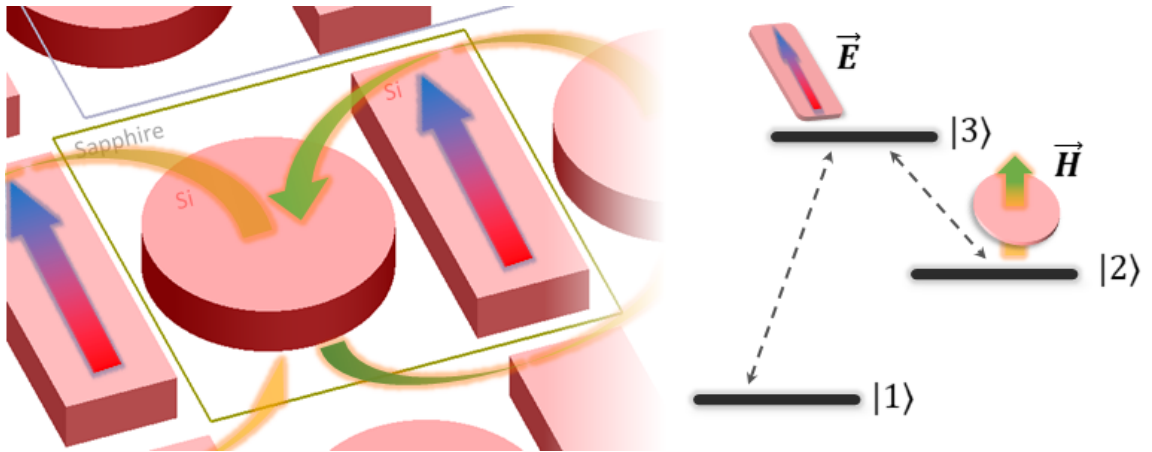


Figure 4.6: EIT analogue metasurface: (Left) Illustration of the spacial arrangement of discs and bars, electric (red to blue gradient) and magnetic (yellow to green gradient) fields, the color gradient illustrates the phase variance. (Right) Energy diagram consisting of a ground non excited state $|1\rangle$, "bright mode" electric dipole excitation $|3\rangle$, and "dark mode" magnetic dipole excitation $|2\rangle$ due to an asymmetric displacement of the disc between two bars.

coherent interaction among the resonators combined with the reduction of absorption loss using a high refractive index material. Evidence to the low absorption loss is displayed in figure (4.1). As expected, the linear phase delay accumulated within the transparency window ($\omega_{transparency} \approx 129THz$) is $\tau_{delay} \approx 3.8ps$ which is equal to a delay of 494cycles (the phase delay was extracted from the phase slope displayed in figure (4.7.c)).

A similar simulation process was done to create EIT analogue spectrums for longer wavelengths centered at 2960nm, 3150nm and 3350nm (for a comparison of design sizes see table C.1 in appendix). Other than expanding the resonators sizes, the Silicon layer height $h = 230nm$ was maintained as well as the interaction lengths scales g_1 and g_2 .

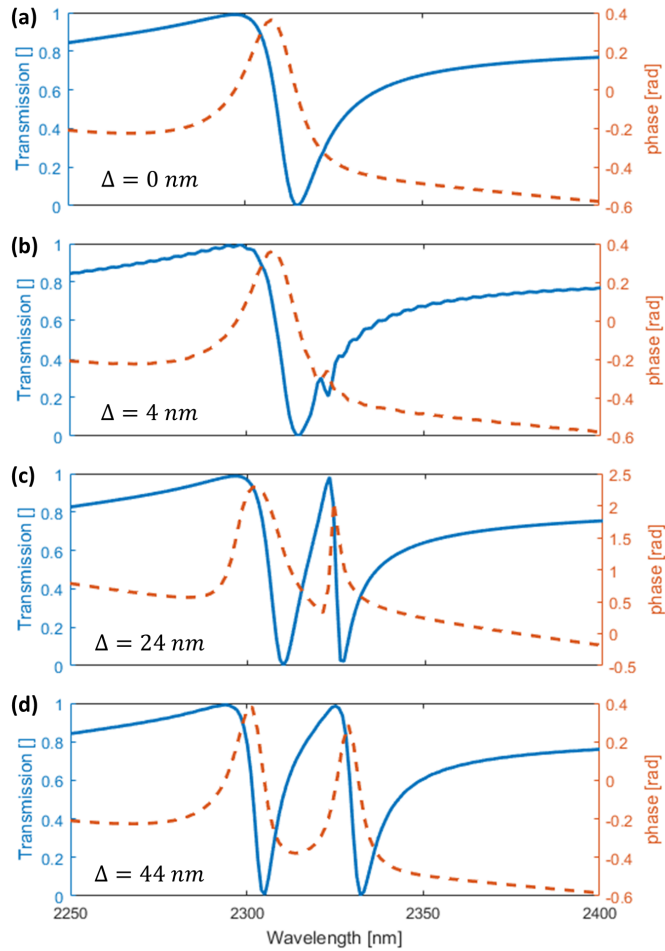


Figure 4.7: Simulation of the EIT analogue design from figure (4.1) of four different detuning levels (Δ). Transmission line (blue) and phase (dashed brown). These plots highlight the importance of a coherent structure, where deviations of 10nm in disc position vary the measured spectrum dramatically.

We can determine the detuning coefficient as $\Delta = g_2 - g_1$; in the symmetric case $\Delta = 0$ while in the EIT analogue case $\Delta = 24nm$. Since it is nearly impossible to simulate a defect placed in a periodic lattice using an FDTD type numerical calculation (we simulate one unit cell with periodic boundary conditions), I have simulated instead, in figure (4.7), how uniform deviations in Δ change the transmission and phase spectrum. This highlights the importance of a coherent structure, i.e the aspiration for minimum deviations between the

geometrical structure of different unit cells. This is, of course, just one example of many possible minor geometrical deviations which may influence the effective electromagnetic properties of the design and cause the loss of the EIT analogue spectrum.

Other weak resonant multipoles can be excited using shorter wavelengths among the discs and bars constituting the EIT design. For instance, figure (4.8) displays field profiles of a very weak Fano-resonance, which originates from interference of an electric quadrupole spanning over the whole unit cell, and a magnetic dipole oriented with the incident magnetic field and located mainly within the disc. An even higher multipole excitation is presented in figure (4.9), where the sample is excited with polarization perpendicular to the bar's long axis. Here the Fano-resonance arises from interference of one high electric multipole excited over the whole unit cell and two high magnetic multipoles excited in the disc and bar separately. These MDRs are excited with nearly identical behaviour in all EIT analogue samples (centered at 2320nm, 2960, 3150nm and 3350nm) with an obvious red-shift as the building block's geometry expands.

4.3 Fabrication process

In the following section, I will elaborate on the fabrication process, which involves several steps. I will first give a brief description of the process and then I will discuss a number of specific issues I dealt with. The process starts by spin coating a positive resist on the designated wafer. In this case a 340nm layer of *ZEP 520A* polymer was used. Since neither the positive resist nor the Silicon layer are conductive, I had to add a conductive thin layer for dissipation of *electron beam* (E-beam) charges from the insulating substrate. In this case I used a 60nm layer of *PMMA Electra 92* as seen in figure (4.10.a). The next step involved E-beam lithography of the intended design using *RAITH150 Two*. The design was built with *RAITH150 software*. In contrast to regular E-beam metasurface designs, here the area to be exposed is not the nano-particle's area but rather the area between the particles as seen in figure (4.10.b). Following the lithography process the exposed areas were removed using a developer. The sample then underwent a *reactive ion etching* (RIE) Bosch process in the *PlasmaTherm SLR 770* machine to etch the 230nm Silicon layer from the exposed areas, as seen in figure (4.10.c). The fabrication process of the metasurface was then complete by removing the remaining polymer as seen in figure (4.10.d).

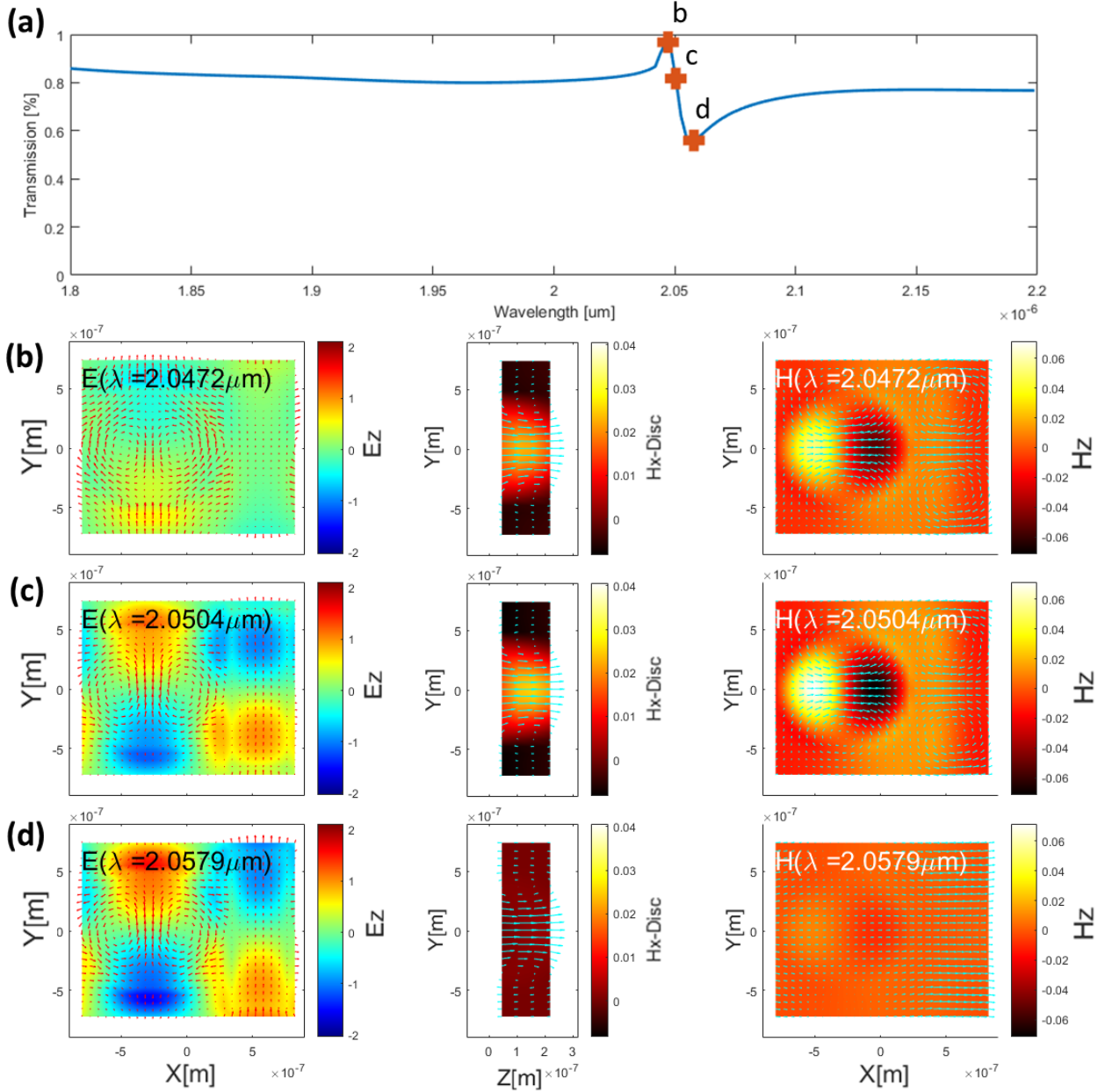


Figure 4.8: Near field profile analysis of the EIT analogue sample centered at 2960nm, asymmetric geometry arrangement ($\Delta = 24\text{nm}$). Simulation for a shorter wavelength excitation centered at $\lambda_r = 2058\text{nm}$. Incident polarization aligned with the bar's long axis. (a) Transmission line (blue), and brown marks that specify the 3 wavelength chosen for field profile display. (b-d) Left: Electric field profile in $z = 46\text{nm}$, colormap indicates $\Re(E_z)$ and red arrows $\Re(E_x, E_y)$. Right: Magnetic field profile in $z = 103\text{nm}$, colormap indicates $\Re(H_z)$ and blue arrows $\Re(H_x, H_y)$. Middle: The magnetic field profile in $x = -436\text{nm}$ (aligned with the center of the disc). The profiles include a caption specifying their excitation wavelength.

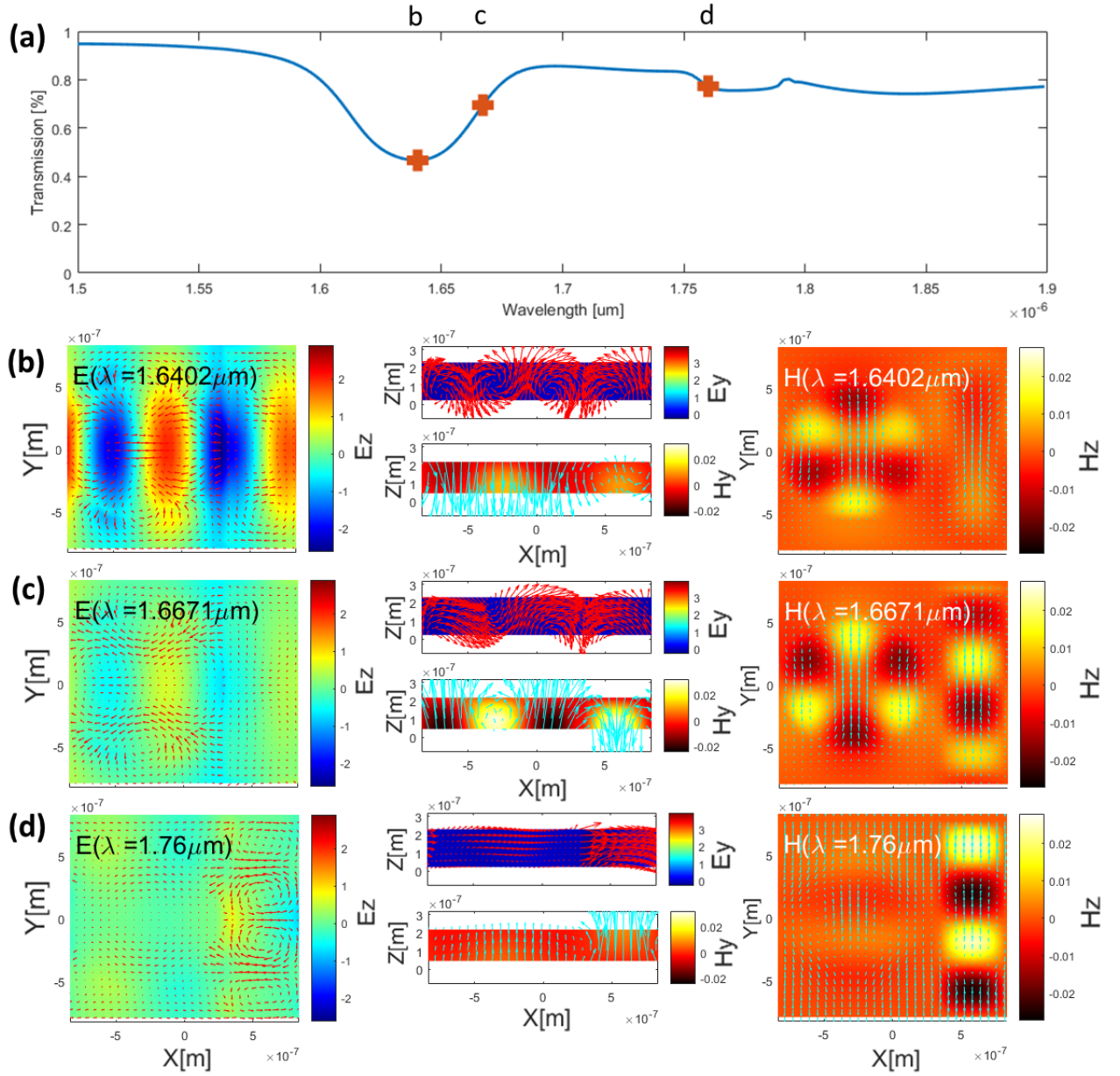


Figure 4.9: Near field profile analysis of the EIT analogue sample centered at 3150nm, asymmetric geometry arrangement ($\Delta = 41.5\text{nm}$). Simulation for a shorter wavelength excitation centered at $\lambda_r = 1640\text{nm}$. Incident polarization perpendicular to the bar's long axis. (a) Transmission line (blue), and brown marks that specify the 3 wavelength chosen for field profile display. (b-d) Left: Electric field profile in $z = 46\text{nm}$, colormap indicates $\Re(E_z)$ and red arrows $\Re(E_x, E_y)$. Right: Magnetic field profile in $z = 103\text{nm}$, colormap indicates $\Re(H_z)$ and blue arrows $\Re(H_x, H_y)$. Middle: Upper display is the electric field profile, and lower display the magnetic field profile in $y = 0$ plane. The profiles include a caption specifying their excitation wavelength.

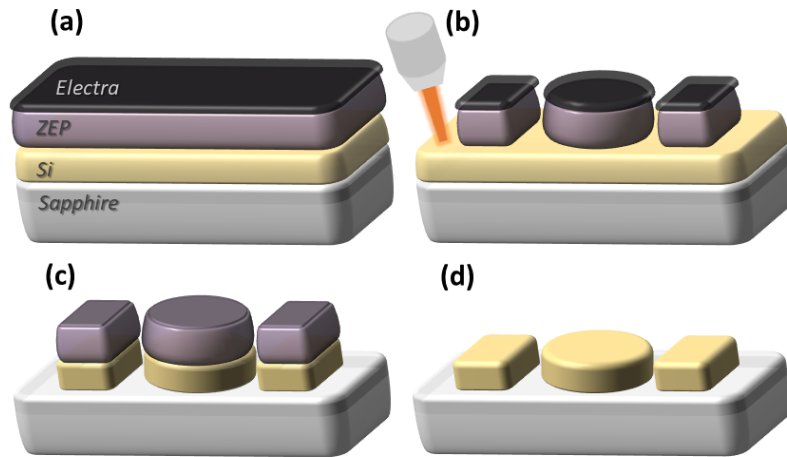


Figure 4.10: Fabrication process illustration - (a) A 230nm Si layer on a Sapphire substrate, spin coated with 340nm ZEP positive resist and 60nm PMMA Electra 92 conductive layer. (b) E-beam lithography exposes the area between the designated particles. (c) A reactive ion etching process is used to etch the exposed Silicon layer until the Sapphire layer is reached. (d) After removing the remaining resist we are left with our metasurface design.

4.3.1 E-beam lithography challenges

After some unsuccessful fabrication attempts I realized that the resist exposure process was never completely localized. This issue became critical when the exposure pattern consisted of complex shapes which require relatively high lithography precision. This challenging issue concerning the E-beam lithography technique caused the particle areas to be small and distorted compared to their design (deviations of up to 50nm), and these changes in particle size caused changes in the interaction lengths and Inevitably different effective electromagnetic properties. To minimize the exposure of neighboring areas I used the highest beam acceleration value available in our nano-center 30kV, with a small 7 μ m aperture. These parameter values gave a \sim 30nm beam size with a beam current of \sim 6pA, what led to a very challenging calibration process. In addition, I used ZEP 520A, a more durable polymer, instead of the commonly used PMMA A4. Furthermore, I came across a proximity effect calculator named *NanoPECS* which I used to reduce the collateral exposure the beam has over its close environment by dividing the design into small polygons and regulating the beam dose factor so it considers the collateral exposure from neighboring polygons. This technique can be very useful when exposing large and complex areas and high precision is needed.

Since the phenomena I am trying to measure depends on coherent interactions among

the "bright" and "dark" mode resonators, the spectrum of this structure is sensitive to lattice perturbations from its edges. These perturbations can lead to strong scattering of light into free space and to broadening of the resonant peak (these effects are absent in the simulations where periodic boundary conditions have been used). Obviously, the fabricated lattice size and the coherence of its resonators are crucial for measuring high Q-factors. Here the *NanoPECS* proximity effect calculations become important again, now in a more macroscopic manner, when the fabricating of coherent structures of over $200\mu m$ are necessary.

4.3.2 RIE process challenges

One last challenging issue concerns finding the appropriate RIE process. Most RIE processes etch bulk material in isotropic directions due to reflections of the accelerated ions from the sample. In order to maintain sharp vertical walls with the appropriate interaction lengths between our building blocks it is necessary to use a unidirectional process like the Bosch process. The Bosch process is a pulsed process alternating repeatedly between two modes, one nearly isotropic plasma etch, and the second is the deposition of a chemically inert passivation layer (similar to Teflon) which protects the entire substrate from further chemical attack and prevents further isotropic etching. After alternating rapidly between the two modes the process succeeds to etch small isotropic steps to create a nearly vertical wall.

Figure (4.11) presents a number of fabricated samples which give good examples to the difficulties mentioned above. For instance, the comparison between figures (b),(e) and (h) show how implementation of the *NanoPECS* proximity effect together with the increasing beam quality and dose tuning, helped fabricate an almost precise metasurface. Another clarifying comparison regarding the etching process can be done between figures (c),(d) of samples that underwent isotropic RIE, to samples etched using a Bosch process that include all the rest ((a)-(b), (e)-(g)). The isotropic process, whether using short (c) or long (d) RIE exposure times, does not preserve the size and interaction lengths of the particles. Moreover, in figure (c) the etching process did not reach the sapphire substrate in areas where the distances between the particles are small. More technical methods regarding the fabrication process are detailed in appendix B.

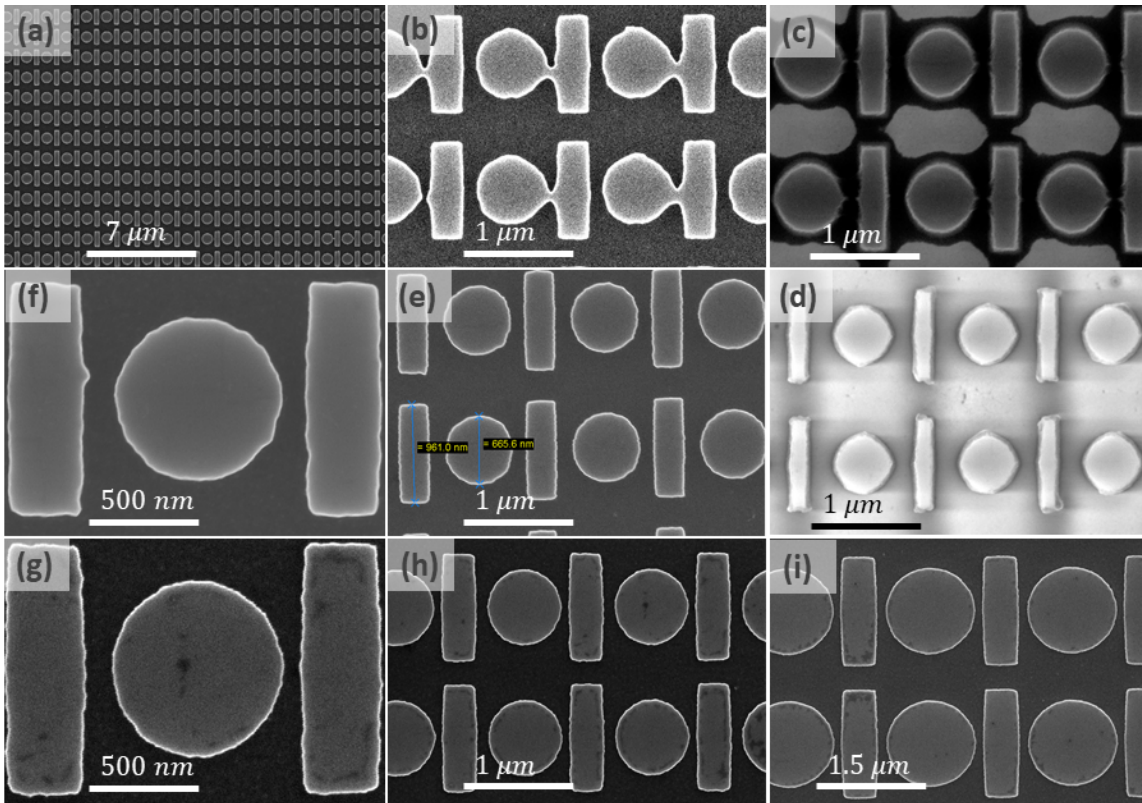


Figure 4.11: SEM images of different fabricated samples: (a) A lattice close up, Dozens of unit cells containing a disk and bar placed alternately in a square lattice. (b) An example of inaccurate fabrication parameters. (c)-(d) Unsuccessfully etched examples from calibration attempts of an isotropic RIE process (while in (h) the *SLR770* Bosch process was used for the same E-beam lithography parameters). (e)-(f) Example of the first successful fabrication processes. (g)-(h) Example of more precise fabrication processes done lately (i) Higher resonance with a larger geometry are easier to fabricate.

4.4 Measurement apparatus

The first attempts to measure the metasurfaces were done using a commercial *Fourier Transform Infrared Spectroscopy* (FTIR) microscope. These FTIR measurements were unsuccessful due to a highly focused, circularly polarised light source. In order to excite coherent resonant oscillations in a relatively large sample area, a polarized plane wave should be used.

4.4.1 The MIRcroscope

The transmission *MIRcroscope* (mid infrared spectroscopic microscope) has been designed to meet the needs of this specific work (see figure (4.12)). It is powered by two independent light sources. One coherent, polarized and collimated MIR plain wave light source designed for carrying out measurements (details in the next paragraph). The second is an incoherent visible white light source, utilized for imaging. The two beams enter the *MIRcroscope* through a 3 axis translation, custom built, sample holder. They are then expanded ($\times 8$) using a telescope and passed through an Iris diaphragm set in the image plane to collect light from the specific designated sample area. The beam is then split using a pellicle beam splitter to redirect the beam to an optical fiber or an imaging system. The imaging is done through a CCD camera and the optical fiber is connected to a commercial spectrometer. The *MIRcroscope* is built as a portable piece (*3Doptix* opto-mechanical components) for the use of a variety of sources and spectrometers.

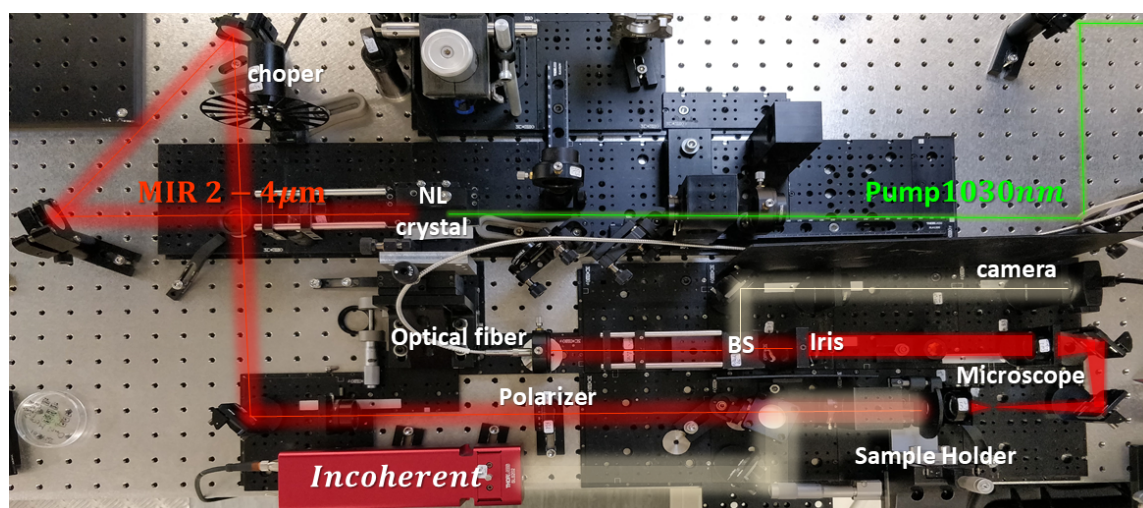


Figure 4.12: The MIRcroscope: a MIR compatible imaging microscope, consists of two light sources, One self generated coherent tunable mid IR collimated plain wave source for measurements, and a second incoherent visible light source for imaging. After propagating through the sample holder the beam is expanded using a telescope, then passed through an Iris to collect light from a certain sample area. The beam is then split using a pellicle beam splitter to an optical fiber and an imaging system.

Measurements were carried out using three main coherent MIR light sources: A femto-second tunable *optical parametric oscillator* (OPO) Idler source using the *ORIA IR Femto-second OPO*. Another, self produced, MIR source used a 1030nm , 6fs , pump and a *MOPO3* crystal enabling a tunable wavelength span of $2 - 4\mu\text{m}$ as illustrated in fig-

ure (4.12). The last coherent laser was a super continuum (SC) laser spanning from 400 – 2500nm.

The spectrometers which were used: *NIRquest512-2.5* - a portable spectrometer, with wavelength range of 900 – 2500nm. This spectrometer was used for all the measurements done under 2500nm. *HORIBA* - not portable, with wavelength range which covers the whole area of interest (2 – 4 μ m). This scanning spectrometer was used for measurements with wavelength higher than 2500nm. Measurements using this spectrometer are modulated using a 200kHz rotating chopper and the *Princeton Lockin amplifier*.

4.5 Measurement results

After the detailed chain of preparation processes, from simulation and fabrication to measurement apparatus and challenges, Here are presented the experimental results for metasurface transmission measurements using the *MIRcroscope*. Although a considerable number of attempts have been made, the anticipated EIT spectrum has not been observed yet. However, referring to the design from figure (4.1), one sample which contains a few 100 \times 100 unit cell lattices (total size of 128 μ m), succeeded to display a Fano-shaped resonance as seen in figure (4.13). Centered at $\lambda_r = 2431nm$ this measured resonance has a Q-factor of 344 extracted from the Fano-shaped fit in figure (4.13.c). The measured resonance was independent of incident power or laser source (*ORIA IR Femto-second OPO* or SC) as can be seen from the comparison of background beam intensities, and respectively, transmission spectrums displayed in figure (4.13.a-b, d-e). In addition, the Fano-resonance displayed delicate tunability when compared to slightly modified geometries as seen in figure (4.13.d). Moreover, as we anticipated, figure (4.13.e) displays a comparison between separate disc and bar lattices with the original geometry stated in figure (4.1) with the same unit cell size as presented by the simulation from figure (4.2). This comparison proves that the Fano-shaped resonance is an emerging property of the interference between the two strongly interacting dipole resonances we discussed in section 4.2.1. In addition, we see a trace of the weak broadband dipole resonance peak, centered at $\sim 2200nm$, with similar shape and position regarding its appearance in the simulated spectrums displayed in figures (4.5, 4.4).

What could possibly be the reason for the absence of an EIT analogue spectrum, and the measured red-shift with respect to its central resonant wavelength? This puzzling question was not answered until I tried to replicate the fabrication process of the sample in question. The same process produced similar geometries but no Fano-resonance were

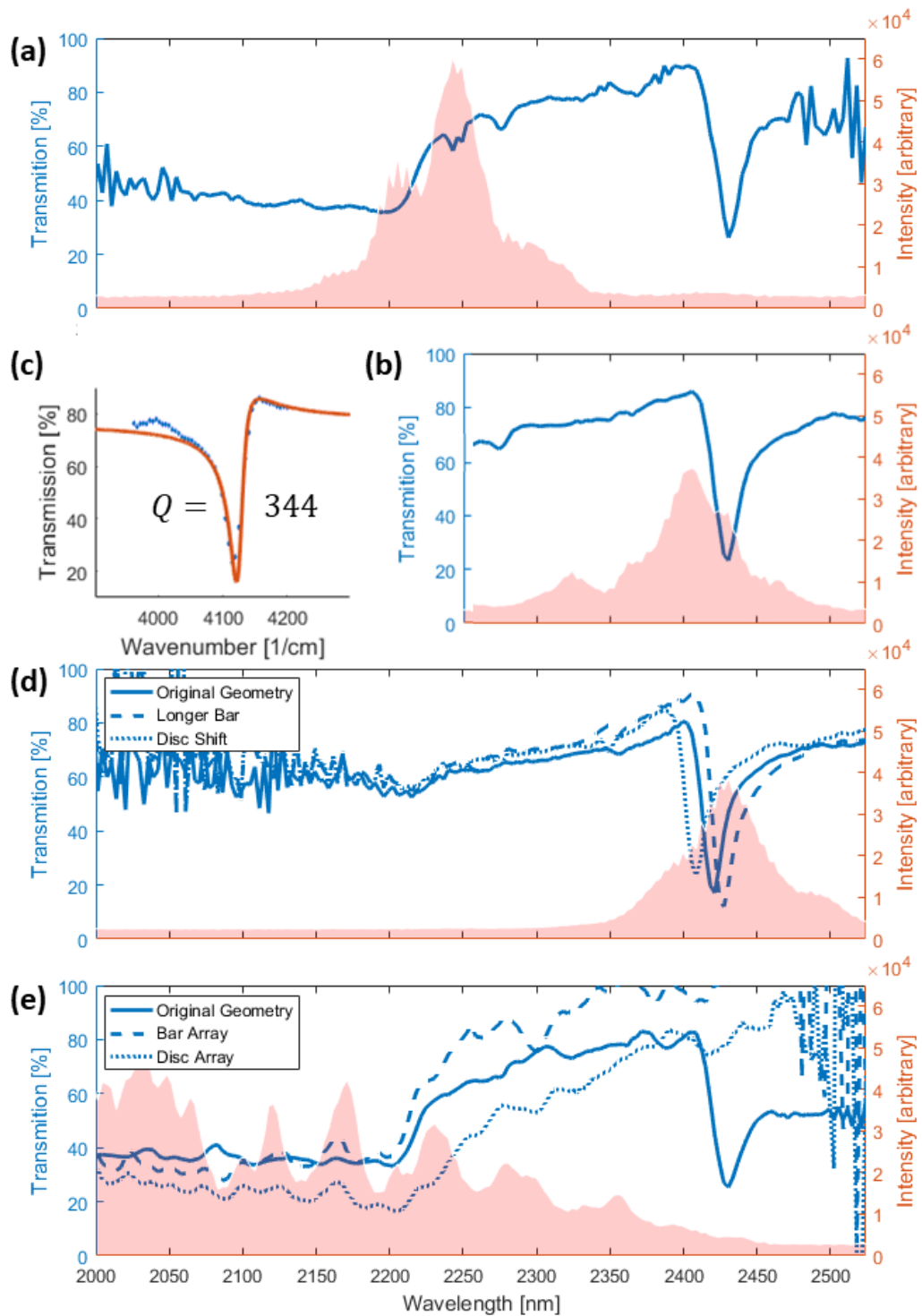


Figure 4.13: A cluster of spectrum measurement plots (a)-(b) Transmission spectrum of a Fano-shaped resonance measured using *ORIA IR Femto-second OPO* with incident beams centred at 2250nm and 2400nm respectively. (c) A Fano-Lorentzian fit for the spectrum measured in figure (b). The extracted Q-factor is 344. Notice the wavelength axis was converted to wavenumber. (d) Geometry comparison with similar designs, but minor geometrical changes. (e) Measurement using the SC laser comparing the original EIT geometry from figure 4.1 to separate disc and bar lattices with same unit cell.

measured. It seems the RIE Bosch process using the *PlasmaTherm SLR 770* is unstable. Furthermore, the process presumably never reached the sapphire stop layer in the dense EIT lattices, although in large exposed areas they definitely did (I verified of that using a Profilometer). Further numerical simulations reveal a match between the Fano-shaped measured resonance to a simulation of a partially etched lattice. Figure (4.14) presents a comparison between the measured spectrum and two simulations. In the first, the lattice is left with a thin layer of 15nm Silicon above the sapphire, and 20nm in the second. The measured spectrum falls right in between the two simulations with a similar line shaped resonance. The unetched Silicon thin layer is presumably not uniform in its depth (a similar non uniform residual layer can be observed in figure (4.11.c)), but this comparison helps direct the improvements needed for our needs.

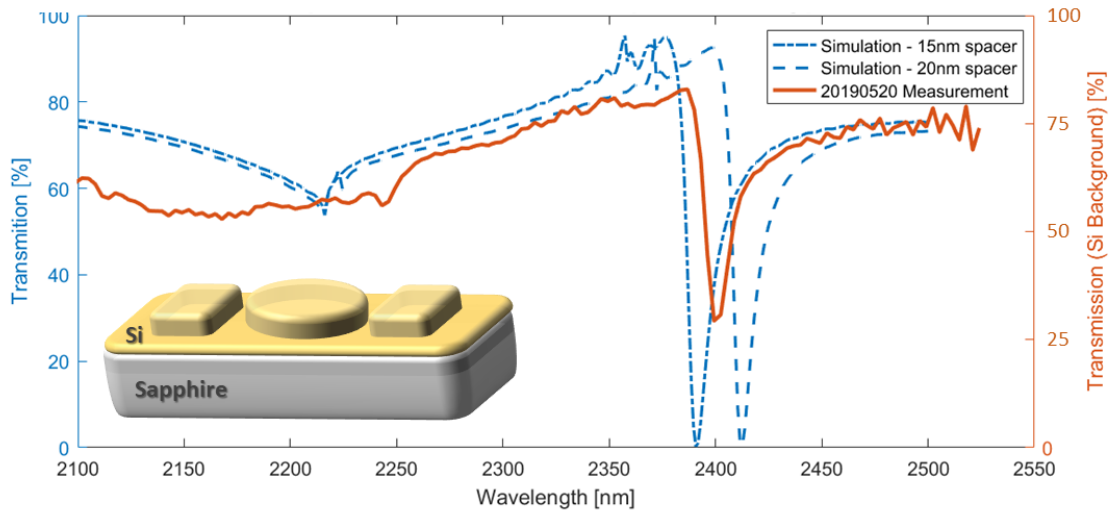


Figure 4.14: Transmission spectrum of measured (orange) and simulated (blue dashed) not fully etched lattices. In addition, an illustration presents the unetched Silicon thin layer on top of the Sapphire substrate.

As mentioned in the end of section 4.2.2, in a similar manner to the Fano-resonance measured before, the longer wavelength EIT analogue designs (centered at 2320nm , 2960 , 3150nm and 3350nm), presented in figure 4.15, display weak Fano-shaped resonances. These measured lattices were fabricated on the same samples as the former not fully etched lattices from before. As a result, I was not surprised to measure weak Fano-resonances with a red-shift of $\sim 330\text{nm}$ with respect to the simulated central wavelength.

When measuring higher multipoles excited by higher frequencies (shorter wavelengths) as investigated in figures (4.8, 4.9), we find an agreement with simulations. Figure (4.16) presents a comparison of measurements to simulations for 3 expanded EIT geometries

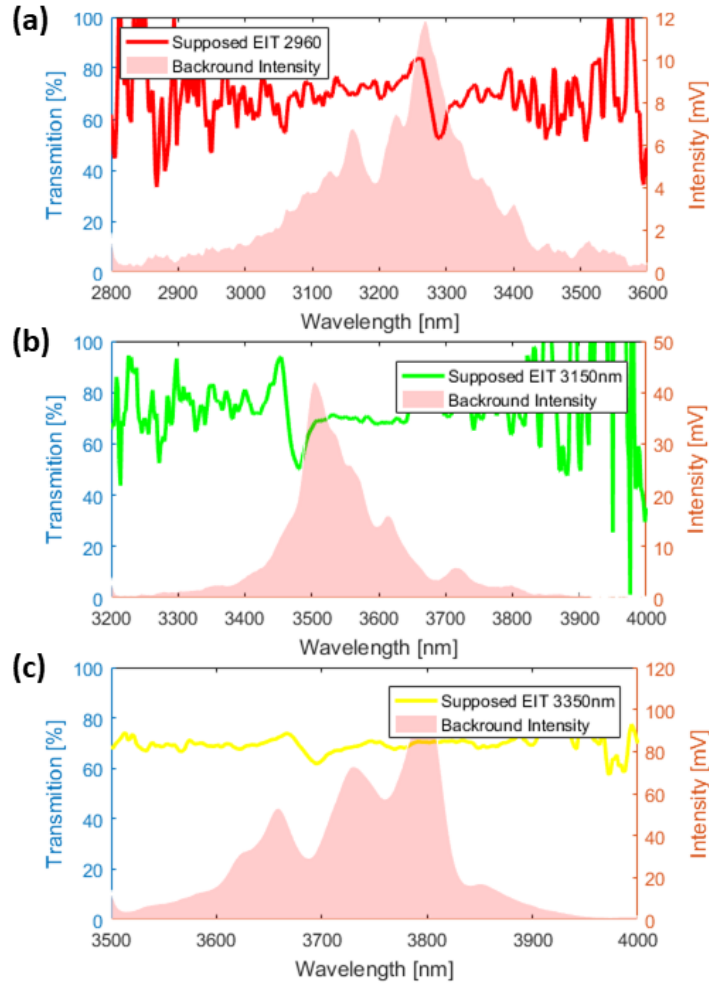


Figure 4.15: Transmission spectrum plots of higher EIT analogue designed samples, using the *HORIBA* spectrometer and the self built tunable MIR source utilizing the *MOPO3* crystal. All three samples display a small Fano-shaped resonance, shifted by $\sim 400\text{nm}$ from its simulated center resonance. (a) Sample designed to resonate in 2960nm but is centered instead in 3290nm . (b) Sample designed to resonate in 3150nm but is centered instead in 3480nm . (c) Sample designed to resonate in 3350nm but is centered instead in 3695nm .

(same as measured in figure (4.15)). In this comparison, other than a constant blue-shift of $\sim 50\text{nm}$ between simulation and measurement, we notice the resonances have a different Fano shape. The calculated Q-factor for these resonances reach 225. I assume the deviation in position and shape originates from the same unstable RIE process mentioned before. This is a satisfying explanation since every MDR whether electric or magnetic is expected to respond differently to changes in boundary conditions and surrounding refractive index. These exciting measurements of high multipole electric and especially magnetic resonances, display the uniqueness of dielectric metasurfaces.

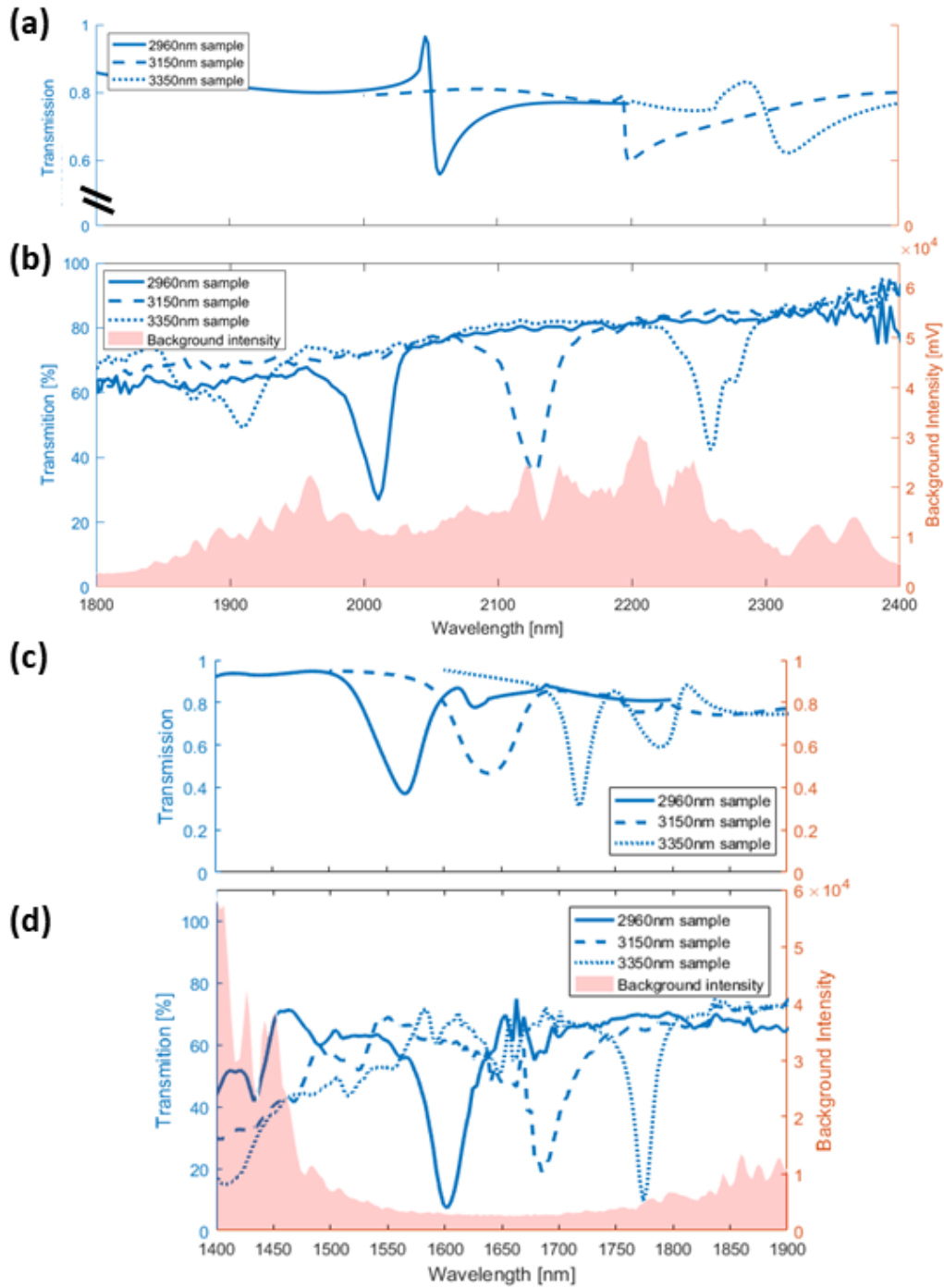


Figure 4.16: Transmission comparison for three different samples (EIT 2960nm, EIT 3150nm and EIT 3350nm from figure (4.15)), between simulations and measurements of high multimode Fano-resonant mechanism. (a) and (b) present simulation and measurements, respectively, for resonant mechanism presented in figure (4.8). Incident beam polarized parallel to the bar's long axis. (c) and (d) present simulation and measurements, respectively, for resonant mechanism presented in figure (4.9). Incident beam polarized perpendicular to the bar's long axis. All measurements were conducted using the *NIRquest* spectrometer and the *SC* source.

5 Conclusions

The work presented here focuses on obtaining MIR metasurface designs with low absorption characteristics. In contrary to previous attempts to create MIR metasurfaces based on LSPRs, we have been focusing our study on a relatively new platform of Silicon based high refractive index nano-structures, which provide high Q-factor Mie resonances with high tunability through pre-design. The analysis is based on extensive numerical simulations - that provide both prediction and also analysis of fabrication defects that have prevented us from observing some of the desired characteristics. The metasurface design, used as a study case, was an EIT analogue spectrum. The underlying mechanism of which is explained in detail. Measurements were carried out using the MIRcroscope, a versatile portable setup, designed for the coherent excitation of the metasurface building blocks. The disagreement between measurements and simulations require further work in order to improve the RIE process. Nevertheless, measurements have demonstrated a Fano resonance, centered at $\lambda_r = 2431\text{nm}$, with a Q-factor of up to 344, way beyond what can be achieved using LSPR based metasurfaces in this spectral range. Further measurements also demonstrate the ability to shift the resonant wavelength farther into the MIR spectrum, as well as fine tuning in a nano-meter scale resolution. Also demonstrated are excitations using higher frequencies, displaying resonances in the NIR to MIR, and arising from a variety of electric and magnetic multipoles as predicted by simulations.

In future work, apart from improving the manufacturing technique, I plan to pursue my research in three main directions: The first is to investigate how Mie resonances in Silicon nano-particles are influenced in the ultra-short regime by pump probe experiments. The pump with excitation energy above the bandgap potential barrier will excite charge carriers to the conduction band, and change the dielectric properties of the material. The probe, which energy is below the bandgap barrier, will detect modifications in the dielectric properties through monitoring of resonance shape and position. Since the magnetic resonances are highly damped due to ohmic losses, as seen in plasmonics, the comparison between the influence of the pump carrier excitation on electric and magnetic resonant mechanisms

could be rather interesting. The second research direction is surface enhanced IR absorption (SEIRA), which includes utilizing the high Q-factor electric and magnetic resonances for MIR biochemical sensing. The Mie resonances can couple to weak molecular vibrational states and induce modulations in the far field spectrum. Interestingly enough, Fano-resonances and EIT analogue spectrums were already demonstrated when coupling such vibrational modes to plasmonic metasurfaces [24]. As mentioned before the introduction of dielectric metasurfaces to the field of biochemical sensing can improve the detection efficiency due to low loss [25]. Primary experiments in a complementary field referred to as surface enhanced Raman spectroscopy (SERS) is presented in appendix A. Third and last is to study the field of nonlinear optics in dielectric metasurfaces, which has traditionally been limited to the visible and NIR spectral regions. Developing and studying efficient frequency conversion methods of MIR radiation to more easily detectable spectral regions will push forward applications that carry information about the chemical composition of materials as well as improve thermal radiation imaging in room temperature. To conclude, the field of dielectric metamaterial in MIR is predicted to be a field with elevated interest for the community in the coming years [10]. Apart from applications mentioned in this paper the MIR spectral range has been hailed as one of the possible directions for integrated photonics [26]. I hope this thesis will be an introduction to many interesting projects and collaborations throughout the research group and beyond.

References

- [1] Max Born and Emil Wolf. Principles of optics, 7th (expanded) edition. *United Kingdom: Press Syndicate of the University of Cambridge*, 461, 1999.
- [2] Christopher L Holloway, Andrew Dienstfrey, Edward F Kuester, John F O’Hara, Abul K Azad, and Antoinette J Taylor. A discussion on the interpretation and characterization of metafilms/metasurfaces: The two-dimensional equivalent of metamaterials. *Metamaterials*, 3(2):100–112, 2009.
- [3] Boris Luk’yanchuk, Nikolay I Zheludev, Stefan A Maier, Naomi J Halas, Peter Nordlander, Harald Giessen, and Chong Tow Chong. The fano resonance in plasmonic nanostructures and metamaterials. *Nature materials*, 9(9):707–715, 2010.
- [4] W Ace Furman. *Electromagnetically Induced Transparency: The Zeeman Method*. PhD thesis, Reed College, 2016.
- [5] Shuang Zhang, Dentcho A Genov, Yuan Wang, Ming Liu, and Xiang Zhang. Plasmon-induced transparency in metamaterials. *Physical review letters*, 101(4):047401, 2008.
- [6] Yujun Zhong, Shyamala Devi Malagari, Travis Hamilton, and Daniel M Wasserman. Review of mid-infrared plasmonic materials. *Journal of Nanophotonics*, 9(1):093791, 2015.
- [7] Aobo Li, Shreya Singh, and Dan Sievenpiper. Metasurfaces and their applications. *Nanophotonics*, 7(6):989–1011, 2018.
- [8] Guixin Li, Shuang Zhang, and Thomas Zentgraf. Nonlinear photonic metasurfaces. *Nature Reviews Materials*, 2(5):1–14, 2017.

- [9] Thierry Talericio and Paolo Biagioni. Semiconductor infrared plasmonics. *Nanophotonics*, 8(6):949–990, 2019.
- [10] Isabelle Staude Jason Valentine Christopher Holloway Igal Brener, Sheng Liu. *Dielectric Metamaterials*. Woodhead Publishing, 2019.
- [11] Craig F Bohren and Donald R Huffman. *Absorption and scattering of light by small particles*. John Wiley & Sons, 2008.
- [12] Jana Olson, Sergio Dominguez-Medina, Anneli Hoggard, Lin-Yung Wang, Wei-Shun Chang, and Stephan Link. Optical characterization of single plasmonic nanoparticles. *Chemical Society Reviews*, 44(1):40–57, 2015.
- [13] Christopher L Holloway, Edward F Kuester, and Andrew Dienstfrey. Characterizing metasurfaces/metafilms: The connection between surface susceptibilities and effective material properties. *IEEE Antennas and Wireless Propagation Letters*, 10:1507–1511, 2011.
- [14] Ugo Fano. Effects of configuration interaction on intensities and phase shifts. *Physical Review*, 124(6):1866, 1961.
- [15] Stephen E Harris. Electromagnetically induced transparency. In *Quantum Electronics and Laser Science Conference*, page QTuB1. Optical Society of America, 1997.
- [16] Nikitas Papasimakis, Vassili A Fedotov, NI Zheludev, and SL Prosvirnin. Metamaterial analog of electromagnetically induced transparency. *Physical Review Letters*, 101(25):253903, 2008.
- [17] Bingxin Han, Xiangjun Li, Chuanshuai Sui, Jinyan Diao, Xufeng Jing, and Zhi Hong. Analog of electromagnetically induced transparency in an e-shaped all-dielectric metasurface based on toroidal dipolar response. *Optical Materials Express*, 8(8):2197–2207, 2018.
- [18] Mengyao Qin, Chengda Pan, Yu Chen, Qiang Ma, Shikang Liu, E Wu, and Bo-tao Wu. Electromagnetically induced transparency in all-dielectric u-shaped silicon metamaterials. *Applied Sciences*, 8(10):1799, 2018.

- [19] Yuanmu Yang, Ivan I Kravchenko, Dayrl P Briggs, and Jason Valentine. All-dielectric metasurface analogue of electromagnetically induced transparency. *Nature communications*, 5(1):1–7, 2014.
- [20] Yuanmu Yang, Wenyi Wang, Abdelaziz Boulesbaa, Ivan I Kravchenko, Dayrl P Briggs, Alexander Poretzky, David Geohegan, and Jason Valentine. Nonlinear fano-resonant dielectric metasurfaces. *Nano letters*, 15(11):7388–7393, 2015.
- [21] Hanzhe Liu, Cheng Guo, Giulio Vampa, Jingyuan Linda Zhang, Tomas Sarmiento, Meng Xiao, Philip H Bucksbaum, Jelena Vučković, Shanhui Fan, and David A Reis. Enhanced high-harmonic generation from an all-dielectric metasurface. *Nature Physics*, 14(10):1006–1010, 2018.
- [22] Manuel Decker and Isabelle Staude. Resonant dielectric nanostructures: a low-loss platform for functional nanophotonics. *Journal of Optics*, 18(10):103001, 2016.
- [23] Arseniy I Kuznetsov, Andrey E Miroshnichenko, Yuan Hsing Fu, JingBo Zhang, and Boris Luk’Yanchuk. Magnetic light. *Scientific reports*, 2:492, 2012.
- [24] Ronen Adato, Alp Artar, Shyamsunder Erramilli, and Hatice Altug. Engineered absorption enhancement and induced transparency in coupled molecular and plasmonic resonator systems. *Nano letters*, 13(6):2584–2591, 2013.
- [25] Ozlem Yavas, Mikael Svedendahl, Paulina Dobosz, Vanesa Sanz, and Romain Quidant. On-a-chip biosensing based on all-dielectric nanoresonators. *Nano letters*, 17(7):4421–4426, 2017.
- [26] Richard Soref. Mid-infrared photonics in silicon and germanium. *Nature photonics*, 4(8):495, 2010.

A Raman scattering from Silicon and Graphene

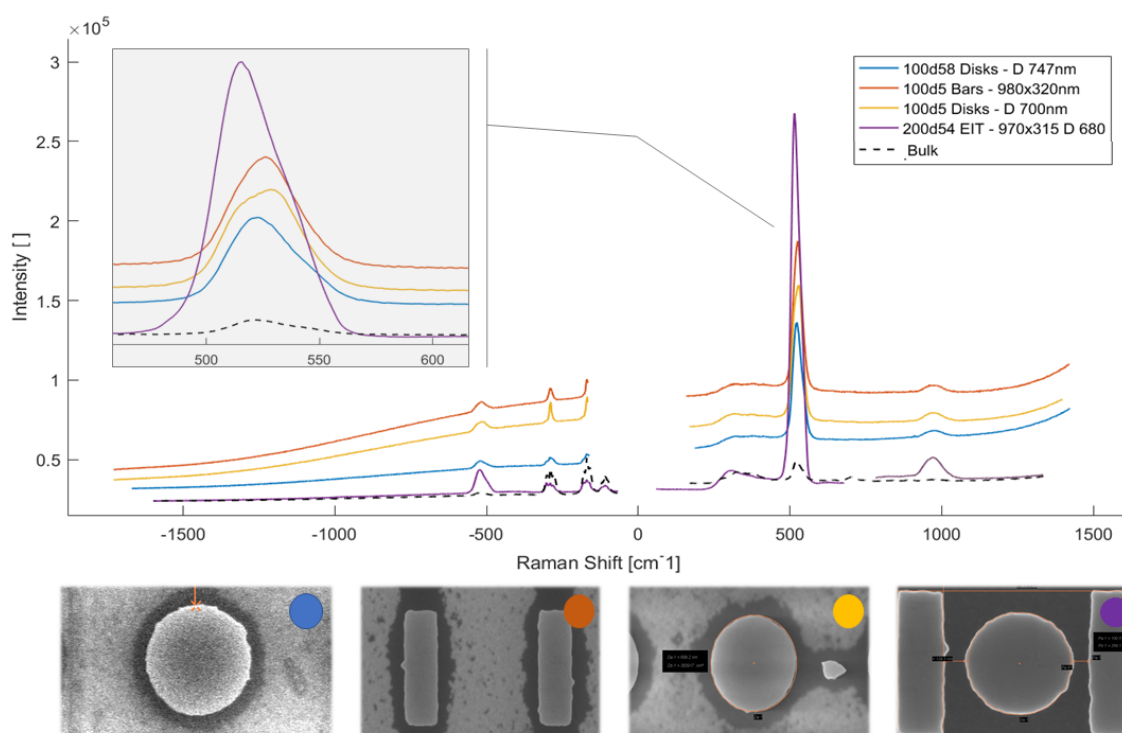


Figure A.1: Raman measurements comparison of Si nanostructures and bulk. A colored circle links between design to spectrum line. Excitation energy 2.33eV. An enhancement factor of $\times 20$ is observed using the metasurface design (purple line) referred to bulk measurements (dashed line). We assume the incident light signal undergoes Near field enhancement due to Mie scattering effects in the nanoparticles.

As a side project during my masters, after I was intrigued by the Idea of using dielectric metasurfaces for enhancement of vibrational spectroscopy in molecules and solids, either by IR absorption or Raman scattering. I decided to conduct spontaneous Raman scattering

measurements of Graphene and Silicon, including my fabricated samples. Interestingly I measured an enhancement factor of $\times 20$ when measuring my EIT sample with respect to bulk Silicon. We assumed the explanation to this enhancement factor comes from Near field enhancement due to Mie scattering effects. En route for surface enhanced Raman spectroscopy (SERS) using dielectric metasurfaces. furthermore I have measured the primary absorption bands of Graphene. Raman measurements of Graphene can be utilized to guess the number of layers by comparing the Raman peak shape to published Raman peak shapes. Here I present measurements done in our lab using a reflection setup I arranged with the help of my colleague Uri Arieli, using an incident continuous wave diode laser centered at 532nm and our *PIXIS* spectrometer.

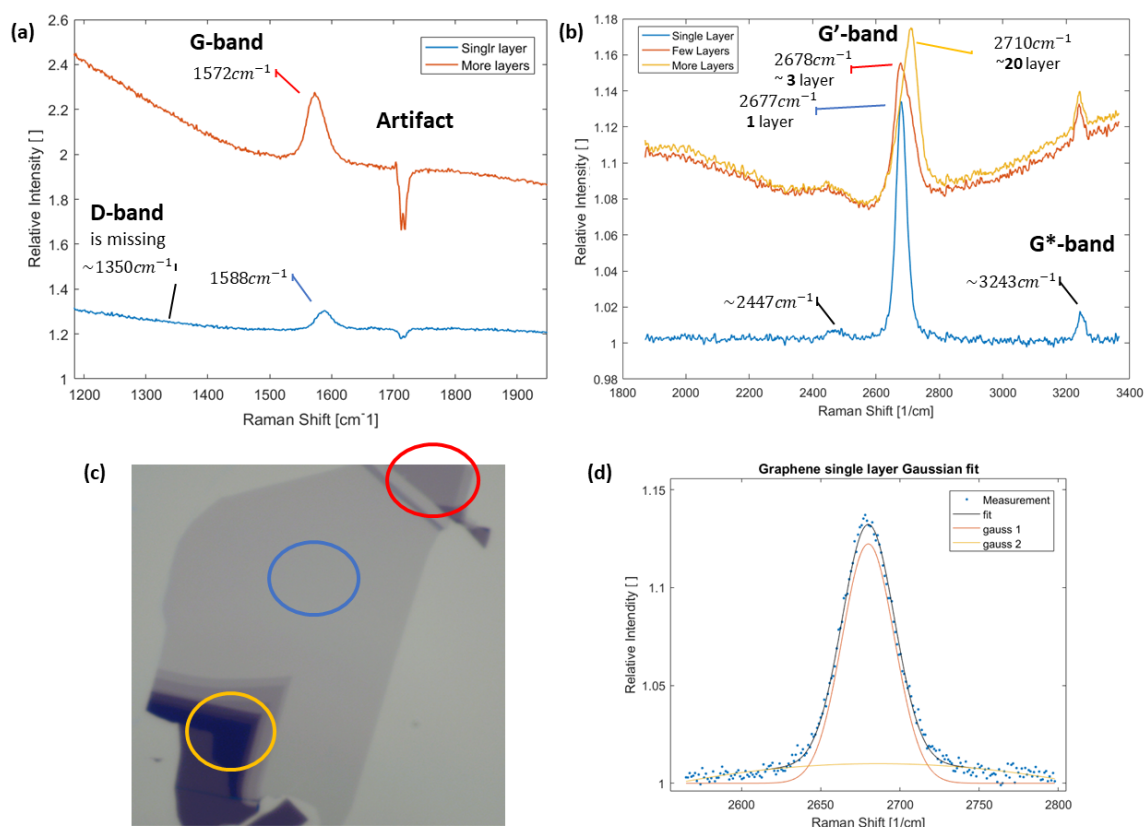


Figure A.2: Raman measurements of single and multi-layered Graphene. (a) Measurements of G-band, no sign for D-band what means the Graphene lattice is free of defects. (b) G'-band measurements, the number of Graphene layers is guessed through comparison to publications. (c) Picture of the Graphene sample with marked areas for measurements with matching color to part b. (d) Gaussian fit for single layer Graphene.

B Methods

B.1 Fabrication recipe

The Preparation process for E-beam lithography starts by cleaning the sample: 2 minute covered in Acetone inside a Sanikator, then same with Isopropanol, dry with nitrogen gun, then bake in 180 degrees for 1 minute. End with Denier-plasma on 50 percent power for 2min. continue with a spin coat process: spin ZEP-520A with 4000 Rpm, then bake in 180 degrees for 2 minutes. On top of the ZEP layer spin PMMA Electra 92, with 2000 Rpm, then bake again in 90 degrees for 2 minutes. Before placing in E-beam it is recommended to clean the sample's lower side with Acetone.

E-beam lithography Writing is conducted using a 30kV, 7 μ m aperture, 7mm Working Distance beam, and a dose of 100pC/mm² deposited in areas with step size of 0.0042 μ m. After extracting the sample from the E-beam, the sample is developed: 20sec in Water to remove the PMMA Electra 92 conducting layer, then 30sec in the ZEP Developer and 20sec Rinse. It is very important not to dry the sample with the nitrogen gun at this point since it sabotages the pattern embedded in the polymer.

Next is the RIE process using the *PlasmaTherm SLR 770* with a process named "UriB-ARB" consisting C4F8/SF6/Ar chemistry. As mentioned before, this process is not yet matured and for that reason will not be specified here. After finishing with the RIE process the remaining polymer is removed using NMP for 2 minutes on a 90 Degrees hotplate, then rinsed in Acetone, Isopropanol, and dried out using the nitrogen gun.

B.2 FDTD simulations

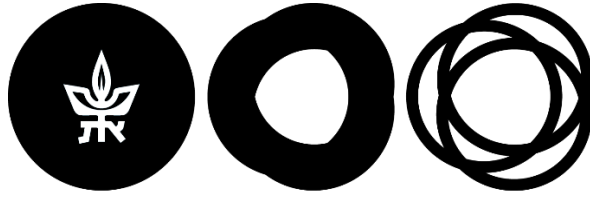
As mentioned, The numerical simulation were conducted using *Lumerical FDTD solutions* software on a single unit cell with periodic boundary conditions in the x-y plane. The top and bottom simulation bounds, which span on a total of 8 μ m, are bound using PML of 8

layers. the geometry of the simulation is as mentioned in table C.1. Source is chosen to be a plain wave, with normal incident and polarized with the long axis of the bar, except for simulations from figure (4.16.c). Total simulation time 20,000fs with a time step of 0.068fs. The far field spectrums are extracted through profile monitors placed in reflection and transmission 200nm distance from the PML bounds. Note the reflection monitor needs to be above the source. Near field profiles are extracted through 3D profile set to capture the E and H fields inside the building blocks and in between them. The specific profiles were processed and plotted via Matlab.

C Designed geometries

**Table C.1: EIT analogue unit cell geometrical designs according to figure (4.1).
All lengths specified in nanometers.**

Center wavelength	Unit Cell	Disc diameter	Bar length×width	Gap right/left
EIT 2320nm	1280×1280	738	1022×347	85.5/109.5
EIT 2960nm	1658×1638	1026	1380×468	85/109
EIT 3150nm	1791×1791	1107	1533×515	63.5/105
EIT 3350nm	1920×1791	1237	1533×520	73/89



TEL AVIV אוניברסיטת
UNIVERSITY תל אביב

הפקולטה למדעים מדויקים ע"ש ריימונד ובברלי סאקלר

בית הספר לפיסיקה ואסטרונומיה

המחלקה לחומר מעובה

מטא-חומרים דיאלקטרים מתכווננים בתחום התת-אדום הבינוני

חיבור זה מוגש כחלק מהדרישות לקבלת תואר 'מוסמך למדעים' באוניברסיטת תל אביב

על ידי

עמרי מירון

עבודה זו הוכנה בהנחיתו של

פרופ' חיים סוכובסקי

מרץ 2020

תקציר

התפתחות יכולות טכנולוגיות מתקדמות לעיצוב חומרים בסקאלות הקטנות מאורך-הגל הולידו את תחום המטא-חומרים. תחום זה חולל מהפכה, בעשרות השנים האחרונות, במחקרים הנוגעים לאינטראקציה בין אור וחומר. שאלות מחקר רבות ומגוונות נחקרו באמצעות מטא-חומרים אלה, בעיקר באזורים הספקטראליים הגלויים לעין ובתחום התת-אדום הקרוב. התחום התת אדום הבינוני, המאפשר יכולות גילוי ייחודיות ממיפוי הרכבים כימיים וביולוגים ועד יכולות גילוי קרינת של גוף שחור, הינו תחום נחקר פחות. תזה זו בוחנת את היכולת ליצור מטא-חומרים עם תהודה בתחום הספקטרוני התת אדום הבינוני. זאת באמצעות גישה חדשה יחסית המכונה מטא-חומרים דיאלקטרים המשתמשת בחומרים שקופים בעלי אינדקס שבירה גבוהה כאבני היסוד שלה. מתיאוריה דרך הדמיות נומריות, תהליך ייצור ומדידה, עבודה זו מתרכזת כמקרה מחקר בתופעה המציגה ספקטרום האנלוגי ל"שקיפות המושרה אלקטרומגנטית" (EIT) בתחום התת-אדום הבינוני. פרט להדמיות שדה קרוב ורחוק המציגות את יחסי הגומלין בין תהודה חשמלית ומגנטית בחומר, התזה מציגה מדידות תהודה עדכניות עם גורם איכות (Q-factor) העולה על 344. כמו גם סדרה של עקומות פאנו-תהודה (Fano-resonance) א-סימטריות הנובעות מההתאבכות בין מגוון מודים מולטיפוליים חשמליים ומגנטיים בחומר. יתר על כן, המדידות מוכיחות יכולת כוונן של אורך הגל המהדהד ברזולוציה גבוהה של עד מספר ננומטרים בודדים, כמו גם שליטה יחסית בסטיות גדולות יותר של מאות ננומטרים תודות להתמקצעות בתהליכי הייצור. בנוסף, התזה דנה באתגרים שעלו מתהליכי הייצור והמדידה, כמו גם המסלולים שנבחרו על מנת להתגבר עליהם.